

Nonlinear performance of continuum mechanics based beam elements focusing on large twisting behaviors

Kyungho Yoon, Phill-Seung Lee*

Division of Ocean Systems Engineering, Korea Advanced Institute of Science and Technology, 291 Daehak-ro, Yuseong-gu, Daejeon 305-701, Republic of Korea

Received 10 May 2014; received in revised form 2 July 2014; accepted 23 July 2014

Available online 1 August 2014

Abstract

In this paper, we present the nonlinear formulation and performance of continuum mechanics based beam elements, in which fully coupled 3D behaviors of stretching, bending, shearing, twisting, and warping are automatically considered. The beam elements are directly degenerated from assemblages of 3D solid elements under the assumptions of Timoshenko beam theory. Therefore, cross-sectional discretization is possible and the elements can model complicated 3D beam geometries including curved and twisted geometries, varying cross-sections, eccentricities, and arbitrary cross-sectional shapes. In particular, the proposed nonlinear formulation can accurately predict large twisting behaviors coupled with stretching, bending, shearing, and warping. Through various numerical examples, we demonstrate the geometric (and material) nonlinear performance of the continuum mechanics based beam elements.

© 2014 Elsevier B.V. All rights reserved.

Keywords: Nonlinear analysis; Finite element method; Beam element; Large twisting; Warping; Lateral buckling

1. Introduction

Beams are widely used structural members in various engineering fields including marine, mechanical, civil engineering, and aerospace engineering fields [1–5]. Recently, beam applications have rapidly extended from classical metallic structures to nano- and bio-structures [6–8], in which the finite element method is a tool that has been dominantly adopted for analysis and design. In order to encompass these new applications, the modeling capability and nonlinear performance have become increasingly important in the finite element analysis of beams.

For a long time, considerable efforts have been made regarding beam theories and the development of beam finite elements; see Refs. [2,3,9–20] for a review of the existing research. Based on classical beam theories, recent works have focused on developing high performance beam finite elements for linear and nonlinear analyses. As a result, the modeling and analysis capabilities have been continuously improved; see Refs. [21–29] for examples. However, compared with other kinematics, relatively small improvements have been made in the large twisting kinematics of beams.

* Corresponding author. Tel.: +82 42 350 1512; fax: +82 42 350 1510.

E-mail address: phillseung@kaist.edu (P.S. Lee).

It is well known that isoparametric beam elements are degenerated from 3D solid elements [1]. Because the beam elements are based on 3D continuum mechanics, they can easily represent general 3D curved geometries including fully coupled complete strains, and the formulation is simple and straightforward. Despite these significant advantages, the original isoparametric beam elements can generally only consider rectangular cross-sections. While several studies have been undertaken in attempts to overcome this limitation in the isoparametric beam elements [4,30–33,27,34], the resulting beams do not clearly model arbitrary beam cross-sections.

Recently, Yoon et al. [35] proposed the concept of continuum mechanics based beam elements, which are degenerated from assemblages of 3D solid elements. Therefore, these beam elements can be considered to be a direct extension of isoparametric beam elements. However, unlike the isoparametric beam elements, the continuum mechanics based beam elements can easily model complicated 3D beam geometries including curved and twisted geometries, varying cross-sections, eccentricity, and arbitrary cross-sectional shapes by incorporating cross-sectional meshes. Furthermore, the beam elements can represent fully coupled behaviors among bending, shearing, stretching, twisting, and warping.

The objective of this paper is to develop a general nonlinear formulation of continuum mechanics based beam elements and present their nonlinear performance focusing on large twisting behaviors. The total Lagrangian formulation is employed and, unlike other beam elements [22–25], the Wagner effect is automatically (implicitly) considered in the beam formulation due to the continuum mechanics based formulation, which results in the capability for large twisting analyses.

The novel aspects of the proposed beam element formulation are summarized as follows:

- The formulation is simple and straightforward.
- Seven degrees of freedom (DOFs) are used at each beam node in order to ensure the inter-elemental continuity of the warping displacements.
- The formulation can manage complicated 3D beam geometries including curved and twisted geometries, varying cross-sections, eccentricity, and arbitrary cross-sectional shapes [35,36].
- The complete tangent stiffness matrix is obtained because the finite rotation of the director vectors is precisely included up to a quadratic order.
- The large twisting and lateral buckling behaviors can be accurately calculated. In the Green–Lagrange strain, the Wagner strain is included implicitly.

In the following sections, the nonlinear kinematics of the continuum mechanics based beams is described. Then, the strain measures are introduced from the given kinematic description and the assumed strain technique used for locking reduction. Next, the incremental equilibrium equation is presented based on the total Lagrangian formulation. Finally, the novelties of the continuum mechanics based beam finite element are demonstrated using well established numerical examples that focus on large twisting behaviors.

2. Large displacement kinematics

The continuum mechanics based beam elements are degenerated from assemblages of 3D solid finite elements [35]. In this section, the large displacement kinematics of the continuum mechanics based beams is presented. In the following formulations, a superscript (or subscript) t is employed to denote time; however, in the static nonlinear analyses considered in this study, t is a dummy variable that indicates the load levels and incremental variables rather than the actual time as in dynamic analyses [1].

Consider a q -node continuum mechanics based beam element that consists of n sub-beams in the configuration at time t , as depicted in Fig. 1. Allowing warping displacements, the geometry interpolation of the sub-beam m (shaded in Fig. 1) is given by

$${}^t\mathbf{x}^{(m)} = \sum_{k=1}^q h_k(r) {}^t\mathbf{x}_k + \sum_{k=1}^q h_k(r) \bar{y}_k^{(m)t} {}^t\mathbf{V}_y^k + \sum_{k=1}^q h_k(r) \bar{z}_k^{(m)t} {}^t\mathbf{V}_z^k + \sum_{k=1}^q h_k(r) f_k^{(m)t} \alpha_k {}^t\mathbf{V}_x^k, \quad (1)$$

in which ${}^t\mathbf{x}^{(m)}$ is the material position vector at time t , $h_k(r)$ is the 1D shape function at beam node k , ${}^t\mathbf{x}_k$ is the position of beam node k at time t , ${}^t\mathbf{V}_x^k$, ${}^t\mathbf{V}_y^k$, and ${}^t\mathbf{V}_z^k$ are the unit director vectors at time t and are normal to each other, $\bar{y}_k^{(m)}$ and $\bar{z}_k^{(m)}$ denote the position in the beam cross-section at beam node k , $f_k^{(m)}$ is the warping function at beam node k , and α_k is the corresponding warping degree of freedom at beam node k at time t ; see Refs. [35,36] for

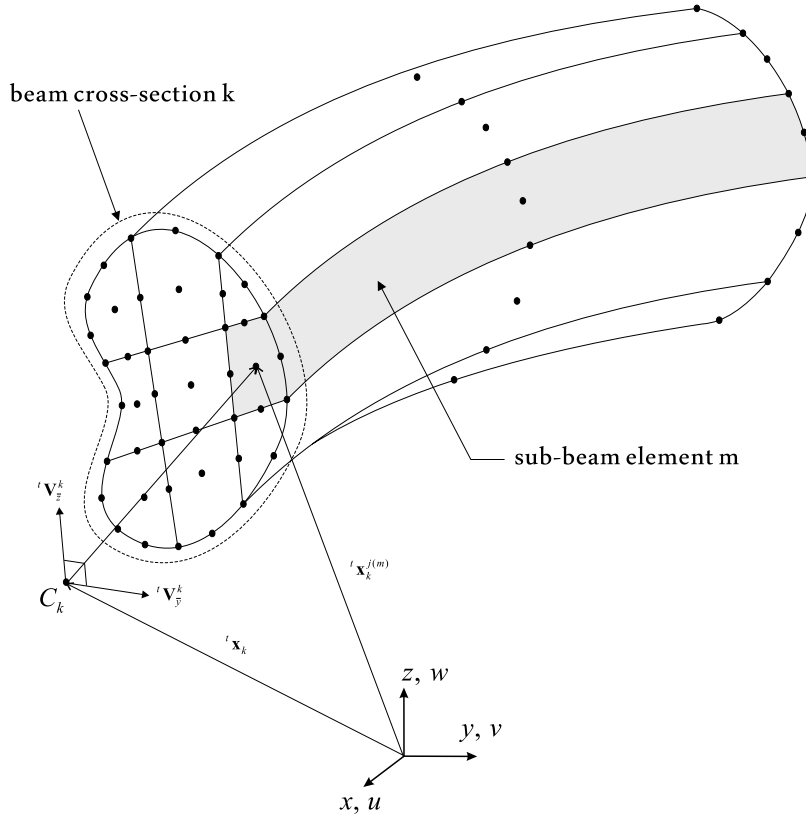


Fig. 1. A 3-node continuum mechanics based beam element with cross-sectional discretization in the configuration at time t . In this figure, the continuum mechanics based beam element consists of 9 sub-beams.

the detailed derivation of Eq. (1). Note that this type of warping model has an intrinsic drawback, that is, the inter-elemental continuity of warping cannot be properly satisfied at nodes where multiple elements are connected and an angle between adjacent elements is not small, see Ref. [28] and therein.

In the continuum mechanics based beam element, a beam cross-section is modeled using a cross-sectional mesh, which is defined using cross-sectional nodes and elements, as seen in Fig. 2. Considering the p -node cross-sectional element m (shaded in Fig. 2) that corresponds to the sub-beam m , the position and warping functions at beam node k are given by

$$\bar{y}_k^{(m)} = \sum_{j=1}^p h_j(s, t) \bar{y}_k^{j(m)}, \quad \bar{z}_k^{(m)} = \sum_{j=1}^p h_j(s, t) \bar{z}_k^{j(m)}, \quad f_k^{(m)} = \sum_{j=1}^p h_j(s, t) f_k^{j(m)}, \quad (2)$$

where $h_j(s, t)$ is the 2D shape function, $\bar{y}_k^{j(m)}$ and $\bar{z}_k^{j(m)}$ denote the position of the cross-sectional node j , and $f_k^{j(m)}$ is the warping value at cross-sectional node j . Note that the number of cross-sectional elements is equal to the number of sub-beams.

In order to represent the material position in the beam cross-section at beam node k , the cross-sectional Cartesian coordinate system is defined using the director vectors ${}^t\mathbf{V}_y^k$ and ${}^t\mathbf{V}_z^k$, and the origin C_k . Note that the position of beam node k , ${}^t\mathbf{x}_k$ is located at the origin C_k . The warping director ${}^t\mathbf{V}_x^k$ in Eq. (1) denotes the warping direction at beam node k at time t and is calculated using ${}^t\mathbf{V}_x^k = {}^t\mathbf{V}_y^k \times {}^t\mathbf{V}_z^k$. The warping values are pre-calculated through solving the St. Venant equations using the finite element procedure with the given cross-sectional meshes, see Refs. [35,36] for more detailed discussions of this method.

For the sub-beam m , the incremental displacement is obtained from the configurations at time t and $t + \Delta t$, as follows

$${}_0\mathbf{u}^{(m)} = {}^{t+\Delta t}\mathbf{x}^{(m)} - {}^t\mathbf{x}^{(m)}. \quad (3)$$

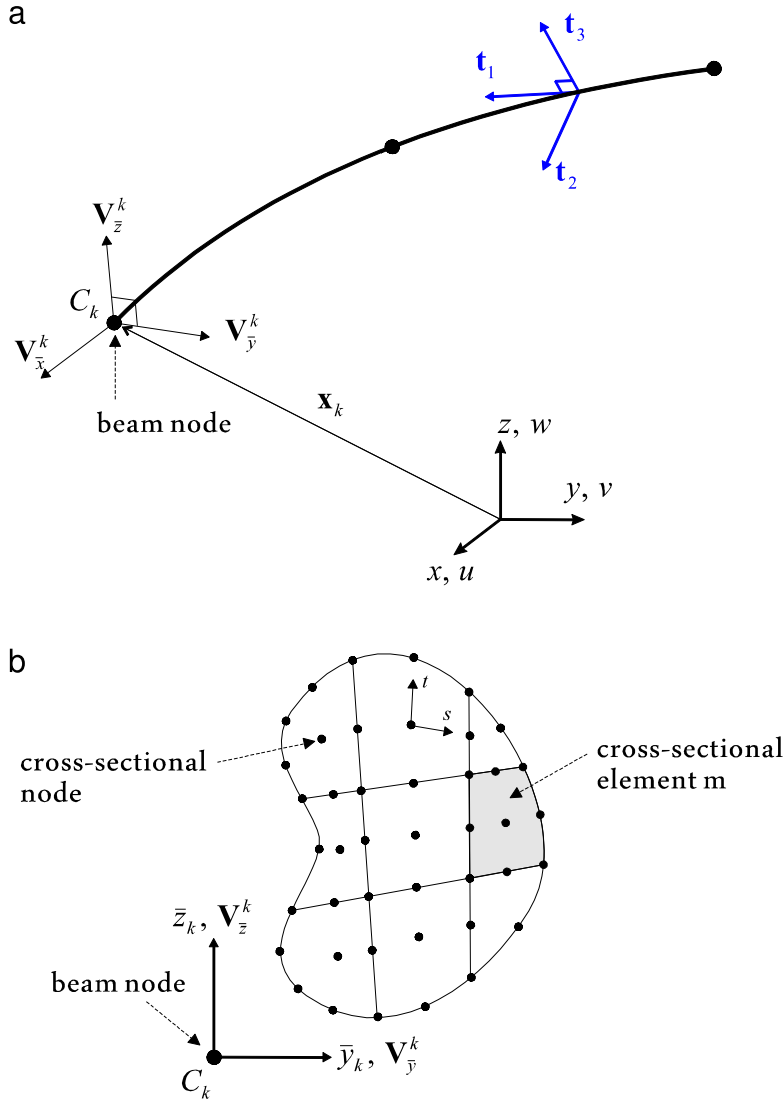


Fig. 2. A continuum mechanics based beam element: (a) beam nodes and coordinate systems used in the beam element and (b) cross-sectional nodes and elements in the cross-sectional mesh.

Using Eq. (1) in Eq. (3), the interpolation of the incremental displacement is obtained by

$$\begin{aligned}
 {}_0\mathbf{u}^{(m)} = & \sum_{k=1}^q h_k(r) {}_0\mathbf{u}_k + \sum_{k=1}^q h_k(r) \bar{y}_k^{(m)} ({}^{t+\Delta t}\mathbf{V}_{\bar{y}}^k - {}^t\mathbf{V}_{\bar{y}}^k) + \sum_{k=1}^q h_k(r) \bar{z}_k^{(m)} ({}^{t+\Delta t}\mathbf{V}_{\bar{z}}^k - {}^t\mathbf{V}_{\bar{z}}^k) \\
 & + \sum_{k=1}^q h_k(r) f_k^{(m)} ({}^{t+\Delta t}\alpha_k {}^{t+\Delta t}\mathbf{V}_{\bar{x}}^k - {}^t\alpha_k {}^t\mathbf{V}_{\bar{x}}^k),
 \end{aligned} \quad (4)$$

where ${}_0\mathbf{u}_k$ is the incremental nodal displacement at beam node k from time t to $t + \Delta t$.

For the parametrization of finite rotations [37–40], the well-known Rodrigues formula is used, as follows

$$\mathbf{R}({}_0\boldsymbol{\theta}^k) = \mathbf{I} + \frac{\sin {}_0\theta^k}{{}_0\theta^k} \hat{\mathbf{R}}({}_0\boldsymbol{\theta}^k) + \frac{1 - \cos {}_0\theta^k}{{}_0\theta^{k2}} \hat{\mathbf{R}}({}_0\boldsymbol{\theta}^k)^2 \quad (5)$$

with ${}^0\boldsymbol{\theta}^k = [{}^0\theta_x^k \quad {}^0\theta_y^k \quad {}^0\theta_z^k]^T$, ${}^0\theta^k = \sqrt{{}^0\theta_x^{k2} + {}^0\theta_y^{k2} + {}^0\theta_z^{k2}}$,

$$\hat{\mathbf{R}}({}^0\boldsymbol{\theta}^k) = \begin{bmatrix} 0 & -{}^0\theta_z^k & {}^0\theta_y^k \\ {}^0\theta_z^k & 0 & -{}^0\theta_x^k \\ -{}^0\theta_y^k & {}^0\theta_x^k & 0 \end{bmatrix}, \quad (6)$$

where ${}^0\theta_x^k$, ${}^0\theta_y^k$, and ${}^0\theta_z^k$ are the incremental Eulerian angles from time t to $t + \Delta t$, and $\hat{\mathbf{R}}$ is the skew-symmetric matrix operator.

Then, the director vectors at time $t + \Delta t$ are defined as

$${}^{t+\Delta t}\mathbf{V}_{\bar{x}}^k = \mathbf{R}({}^0\boldsymbol{\theta}^k){}^t\mathbf{V}_{\bar{x}}^k, \quad {}^{t+\Delta t}\mathbf{V}_{\bar{y}}^k = \mathbf{R}({}^0\boldsymbol{\theta}^k){}^t\mathbf{V}_{\bar{y}}^k, \quad \text{and} \quad {}^{t+\Delta t}\mathbf{V}_{\bar{z}}^k = \mathbf{R}({}^0\boldsymbol{\theta}^k){}^t\mathbf{V}_{\bar{z}}^k. \quad (7)$$

Using Eq. (7) in Eq. (4), we can obtain the following

$$\begin{aligned} {}^0\mathbf{u}^{(m)} &= \sum_{k=1}^q h_k(r){}_0\mathbf{u}_k + \sum_{k=1}^q h_k(r)\bar{y}_k^{(m)}(\mathbf{R}({}^0\boldsymbol{\theta}^k) - \mathbf{I})^t\mathbf{V}_{\bar{y}}^k + \sum_{k=1}^q h_k(r)\bar{z}_k^{(m)}(\mathbf{R}({}^0\boldsymbol{\theta}^k) - \mathbf{I})^t\mathbf{V}_{\bar{z}}^k \\ &\quad + \sum_{k=1}^q h_k(r)f_k^{(m)}({}_0\alpha_k\mathbf{R}({}^0\boldsymbol{\theta}^k) + {}^t\alpha_k(\mathbf{R}({}^0\boldsymbol{\theta}^k) - \mathbf{I}))^t\mathbf{V}_{\bar{x}}^k, \end{aligned} \quad (8)$$

in which ${}_0\alpha_k$ is the incremental warping degree of freedom at beam node k .

Applying the Taylor expansion to Eq. (5), the finite rotation tensor $\mathbf{R}({}^0\boldsymbol{\theta}^k)$ can be represented using a polynomial function with respect to the incremental Eulerian angle vector ${}^0\boldsymbol{\theta}^k$

$$\mathbf{R}({}^0\boldsymbol{\theta}^k) = \mathbf{I} + \hat{\mathbf{R}}({}^0\boldsymbol{\theta}^k) + \frac{1}{2!}\hat{\mathbf{R}}({}^0\boldsymbol{\theta}^k)^2 + \frac{1}{3!}\hat{\mathbf{R}}({}^0\boldsymbol{\theta}^k)^3 + \frac{1}{4!}\hat{\mathbf{R}}({}^0\boldsymbol{\theta}^k)^4 + \dots \quad (9)$$

Substituting Eq. (9) into Eq. (8) and using the second order approximation for the finite rotation, the incremental displacement in Eq. (8) becomes

$${}^0\mathbf{u}^{(m)} \approx {}^0\mathbf{u}_1^{(m)} + {}^0\mathbf{u}_2^{(m)} \quad (10)$$

with

$$\begin{aligned} {}^0\mathbf{u}_1^{(m)} &= \sum_{k=1}^q h_k(r){}_0\mathbf{u}_k + \sum_{k=1}^q h_k(r)\bar{y}_k^{(m)}\hat{\mathbf{R}}({}^0\boldsymbol{\theta}^k){}^t\mathbf{V}_{\bar{y}}^k + \sum_{k=1}^q h_k(r)\bar{z}_k^{(m)}\hat{\mathbf{R}}({}^0\boldsymbol{\theta}^k){}^t\mathbf{V}_{\bar{z}}^k \\ &\quad + \sum_{k=1}^q h_k(r)f_k^{(m)}[{}_0\alpha_k\mathbf{I} + {}^t\alpha_k\hat{\mathbf{R}}({}^0\boldsymbol{\theta}^k)]^t\mathbf{V}_{\bar{x}}^k, \end{aligned} \quad (11)$$

$$\begin{aligned} {}^0\mathbf{u}_2^{(m)} &= \frac{1}{2} \sum_{k=1}^q h_k(r)\bar{y}_k^{(m)}\hat{\mathbf{R}}({}^0\boldsymbol{\theta}^k)^2{}^t\mathbf{V}_{\bar{y}}^k + \frac{1}{2} \sum_{k=1}^q h_k(r)\bar{z}_k^{(m)}\hat{\mathbf{R}}({}^0\boldsymbol{\theta}^k)^2{}^t\mathbf{V}_{\bar{z}}^k \\ &\quad + \sum_{k=1}^q h_k(r)f_k^{(m)} \left[{}_0\alpha_k\hat{\mathbf{R}}({}^0\boldsymbol{\theta}^k) + \frac{1}{2}{}^t\alpha_k\hat{\mathbf{R}}({}^0\boldsymbol{\theta}^k)^2 \right]^t\mathbf{V}_{\bar{x}}^k, \end{aligned} \quad (12)$$

in which ${}^0\mathbf{u}_1^{(m)}$ and ${}^0\mathbf{u}_2^{(m)}$ are the linear and quadratic parts, respectively, in the incremental displacement.

In the incremental displacement in Eq. (10), seven DOFs (three translations, three rotations, and one warping DOF) are employed at beam node k using the nodal DOFs vector:

$${}^0\mathbf{U}_k = [{}^0u_k \quad {}^0v_k \quad {}^0w_k \quad | \quad {}^0\theta_x^k \quad {}^0\theta_y^k \quad {}^0\theta_z^k \quad | \quad {}^0\alpha_k]^T, \quad (13)$$

and the DOFs vector of the q -node beam element is as follows

$${}^0\mathbf{U} = [{}^0\mathbf{U}_1^T \quad {}^0\mathbf{U}_2^T \quad \dots \quad {}^0\mathbf{U}_q^T]^T. \quad (14)$$

Then, ${}_0\mathbf{u}_1^{(m)}$ is represented in terms of the nodal DOFs vector

$${}_0\mathbf{u}_1^{(m)} = \begin{bmatrix} \mathbf{L}_1^{(m)} & \mathbf{L}_2^{(m)} & \cdots & \mathbf{L}_q^{(m)} \end{bmatrix} {}_0\mathbf{U} = \mathbf{L}^{(m)} {}_0\mathbf{U} \quad (15)$$

with

$$\mathbf{L}_k^{(m)} = h_k(r) \left[\mathbf{I} - \left(\bar{y}_k^{(m)} \hat{\mathbf{R}}(t \mathbf{V}_{\bar{y}}^k) + \bar{z}_k^{(m)} \hat{\mathbf{R}}(t \mathbf{V}_{\bar{z}}^k) + f_k^{(m)t} \alpha_k \hat{\mathbf{R}}(t \mathbf{V}_{\bar{x}}^k) \right) f_k^{(m)}(s, t) {}^t\mathbf{V}_{\bar{x}}^k \right]. \quad (16)$$

Also, ${}_0\mathbf{u}_2^{(m)}$ is given by

$${}_0\mathbf{u}_2^{(m)} = \begin{bmatrix} {}_0u_2^{(m)} \\ {}_0v_2^{(m)} \\ {}_0w_2^{(m)} \end{bmatrix} = \frac{1}{2} \begin{bmatrix} {}_0\mathbf{U}^T {}_1\mathbf{Q}^{(m)} {}_0\mathbf{U} \\ {}_0\mathbf{U}^T {}_2\mathbf{Q}^{(m)} {}_0\mathbf{U} \\ {}_0\mathbf{U}^T {}_3\mathbf{Q}^{(m)} {}_0\mathbf{U} \end{bmatrix} \quad (17)$$

with

$${}_i\mathbf{Q}^{(m)} = \begin{bmatrix} {}_i\mathbf{Q}_1^{(m)} & {}_i\mathbf{Q}_2^{(m)} & \cdots & {}_i\mathbf{Q}_q^{(m)} \end{bmatrix}, \quad i = 1, 2, 3, \quad (18)$$

in which

$${}_i\mathbf{Q}_k^{(m)} = h_k(r) \begin{bmatrix} \mathbf{0} & \mathbf{0} & \mathbf{0} \\ \mathbf{0} & \bar{y}_k^{(m)} \boldsymbol{\Psi}_i(t \mathbf{V}_{\bar{y}}^k) + \bar{z}_k^{(m)} \boldsymbol{\Psi}_i(t \mathbf{V}_{\bar{z}}^k) + f_k^{(m)t} \alpha_k \boldsymbol{\Psi}_i(t \mathbf{V}_{\bar{x}}^k) - f_k^{(m)} \hat{\mathbf{R}}_i(t \mathbf{V}_{\bar{x}}^k)^T \\ \mathbf{0} & -f_k^{(m)} \hat{\mathbf{R}}_i(t \mathbf{V}_{\bar{x}}^k) & 0 \end{bmatrix} \quad (19)$$

with

$$\begin{aligned} \boldsymbol{\Psi}_1(\mathbf{x}) &= \frac{1}{2} \begin{bmatrix} 0 & x_2 & x_3 \\ x_2 & -2x_1 & 0 \\ x_3 & 0 & -2x_1 \end{bmatrix}, & \boldsymbol{\Psi}_2(\mathbf{x}) &= \frac{1}{2} \begin{bmatrix} -2x_2 & x_1 & 0 \\ x_1 & 0 & x_3 \\ 0 & x_3 & -2x_2 \end{bmatrix}, \\ \boldsymbol{\Psi}_3(\mathbf{x}) &= \frac{1}{2} \begin{bmatrix} -2x_3 & 0 & x_1 \\ 0 & -2x_3 & x_2 \\ x_1 & x_2 & 0 \end{bmatrix}, \end{aligned} \quad (20)$$

and

$$\hat{\mathbf{R}}_1(\mathbf{x}) = \begin{bmatrix} 0 & -x_3 & x_2 \end{bmatrix}, \quad \hat{\mathbf{R}}_2(\mathbf{x}) = \begin{bmatrix} x_3 & 0 & -x_1 \end{bmatrix}, \quad \text{and} \quad \hat{\mathbf{R}}_3(\mathbf{x}) = \begin{bmatrix} -x_2 & x_1 & 0 \end{bmatrix}. \quad (21)$$

The variations of the incremental displacements are given by:

$$\delta {}_0\mathbf{u}_1^{(m)} = \mathbf{L}^{(m)} \delta {}_0\mathbf{U} \quad \text{and} \quad \delta {}_0\mathbf{u}_2^{(m)} = \begin{bmatrix} \delta {}_0u_2^{(m)} \\ \delta {}_0v_2^{(m)} \\ \delta {}_0w_2^{(m)} \end{bmatrix} = \begin{bmatrix} \delta {}_0\mathbf{U}^T {}_1\mathbf{Q}^{(m)} {}_0\mathbf{U} \\ \delta {}_0\mathbf{U}^T {}_2\mathbf{Q}^{(m)} {}_0\mathbf{U} \\ \delta {}_0\mathbf{U}^T {}_3\mathbf{Q}^{(m)} {}_0\mathbf{U} \end{bmatrix}. \quad (22)$$

3. Green–Lagrange strains

The covariant Green–Lagrange strain tensor ${}^t_0\varepsilon_{ij}^{(m)}$ for the sub-beam m at the configuration at time t , referred to the configuration at time 0, is defined as follows

$${}^t_0\varepsilon_{ij}^{(m)} = \frac{1}{2} ({}^t\mathbf{g}_i^{(m)} \cdot {}^t\mathbf{g}_j^{(m)} - {}_0\mathbf{g}_i^{(m)} \cdot {}_0\mathbf{g}_j^{(m)}) \quad \text{with} \quad {}^t\mathbf{g}_i^{(m)} = \frac{\partial {}^t\mathbf{x}^{(m)}}{\partial r_i}, \quad (23)$$

in which $r_1 = 1$, $r_2 = 2$, and $r_3 = 3$. Since cross-sectional deformations are not allowed in Timoshenko beam theory, in the beam formulation, only five strain components (${}^t_0\varepsilon_{11}^{(m)}$, ${}^t_0\varepsilon_{12}^{(m)}$, ${}^t_0\varepsilon_{21}^{(m)}$, ${}^t_0\varepsilon_{13}^{(m)}$, and ${}^t_0\varepsilon_{31}^{(m)}$) are considered; that is, $(i, j) \in \{(1, 1), (1, 2), (2, 1), (1, 3), (3, 1)\}$. The other strain components (${}^t_0\varepsilon_{22}^{(m)}$, ${}^t_0\varepsilon_{33}^{(m)}$, ${}^t_0\varepsilon_{23}^{(m)}$, and ${}^t_0\varepsilon_{32}^{(m)}$) are zero. It is important to note that, when the covariant base vector ${}^t\mathbf{g}_i^{(m)}$ is calculated, the warping effect in the geometry

interpolation in Eq. (1) should be considered. Otherwise, the Wagner strain term cannot be correctly included in the beam formulation, see [Appendix](#).

The local Green–Lagrange strain tensor ${}^t\bar{\varepsilon}_{ij}^{(m)}$ defined in the local Cartesian coordinate system in [Fig. 2\(a\)](#) is calculated using the following equation:

$${}^t\bar{\varepsilon}_{ij}^{(m)}({}^0\mathbf{t}_i \otimes {}^0\mathbf{t}_j) = {}^t\varepsilon_{kl}^{(m)}({}^0\mathbf{g}^{k(m)} \otimes {}^0\mathbf{g}^{l(m)}), \quad (24)$$

where the base vectors for the local Cartesian coordinate system are given by:

$${}^0\mathbf{t}_1 = h_k(r){}^0\mathbf{V}_{\bar{x}}^k, \quad {}^0\mathbf{t}_2 = h_k(r){}^0\mathbf{V}_{\bar{y}}^k \quad \text{and} \quad {}^0\mathbf{t}_3 = h_k(r){}^0\mathbf{V}_{\bar{z}}^k. \quad (25)$$

Here, the five non-zero components in the local Green–Lagrange strain tensor are also considered: ${}^t\varepsilon_{11}^{(m)}$, ${}^t\varepsilon_{12}^{(m)}$, ${}^t\varepsilon_{21}^{(m)}$, ${}^t\varepsilon_{13}^{(m)}$, and ${}^t\varepsilon_{31}^{(m)}$. In Eq. (24), the contravariant base vectors ${}^0\mathbf{g}^{i(m)}$ are calculated using

$${}^0\mathbf{g}^{i(m)} \cdot {}^0\mathbf{g}_j^{(m)} = \delta_j^i, \quad (26)$$

in which δ_j^i denotes the Kronecker delta ($\delta_j^i = 1$ if $i = j$, and 0 otherwise).

Substituting Eq. (1) into Eq. (23), the incremental covariant Green–Lagrange strain for the sub-beam m is derived as follows

$${}^0\varepsilon_{ij}^{(m)} = {}^{t+\Delta t}{}^0\varepsilon_{ij}^{(m)} - {}^t\varepsilon_{ij}^{(m)} = \frac{1}{2}({}^t\mathbf{g}_j^{(m)} \cdot {}^0\mathbf{u}_{,i}^{(m)} + {}^t\mathbf{g}_i^{(m)} \cdot {}^0\mathbf{u}_{,j}^{(m)} + {}^0\mathbf{u}_{,i}^{(m)} \cdot {}^0\mathbf{u}_{,j}^{(m)}) \quad \text{with} \quad {}^0\mathbf{u}_{,i}^{(m)} = \frac{\partial {}^0\mathbf{u}^{(m)}}{\partial r_i}. \quad (27)$$

Retaining only the strain terms up to the quadratic order with respect to the nodal DOFs through substituting Eq. (10) into Eq. (27), the incremental covariant Green–Lagrange strain can be decomposed into the following equation

$${}^0\varepsilon_{ij}^{(m)} \approx {}^0e_{ij}^{(m)} + {}^0\eta_{ij}^{(m)} + {}^0\kappa_{ij}^{(m)} \quad (28)$$

with

$$\begin{aligned} {}^0e_{ij}^{(m)} &= \frac{1}{2}({}^t\mathbf{g}_j^{(m)} \cdot {}^0\mathbf{u}_{1,i}^{(m)} + {}^t\mathbf{g}_i^{(m)} \cdot {}^0\mathbf{u}_{1,j}^{(m)}), & {}^0\eta_{ij}^{(m)} &= \frac{1}{2}{}^0\mathbf{u}_{1,i}^{(m)} \cdot {}^0\mathbf{u}_{1,j}^{(m)} \quad \text{and} \\ {}^0\kappa_{ij}^{(m)} &= \frac{1}{2}({}^t\mathbf{g}_j^{(m)} \cdot {}^0\mathbf{u}_{2,i}^{(m)} + {}^t\mathbf{g}_i^{(m)} \cdot {}^0\mathbf{u}_{2,j}^{(m)}), \end{aligned} \quad (29)$$

where ${}^0e_{ij}^{(m)}$ and ${}^0\eta_{ij}^{(m)}$ denote the linear and nonlinear terms, respectively, due to the linear incremental displacement ${}^0\mathbf{u}_1^{(m)}$ in Eq. (11), and ${}^0\kappa_{ij}^{(m)}$ denotes the nonlinear term that results from the quadratic incremental displacement ${}^0\mathbf{u}_2^{(m)}$ in Eq. (12).

Note that Eqs. (28) and (29) contain all strain terms up to the quadratic order with respect to the nodal DOFs, which therefore leads to a complete expression of the tangent stiffness matrix.

Using Eqs. (15) and (17) in Eq. (29), the following relations between the incremental strains and incremental nodal displacements are obtained

$${}^0e_{ij}^{(m)} = \frac{1}{2}({}^t\mathbf{g}_j^{(m)} \cdot \mathbf{L}_{,i}^{(m)} + {}^t\mathbf{g}_i^{(m)} \cdot \mathbf{L}_{,j}^{(m)})_0 \mathbf{U} = \mathbf{B}_{ij}^{(m)}{}_0 \mathbf{U}, \quad (30a)$$

$${}^0\eta_{ij}^{(m)} = \frac{1}{2}{}_0 \mathbf{U}^T (\mathbf{L}_{,i}^{(m)T} \mathbf{L}_{,j}^{(m)})_0 \mathbf{U} = \frac{1}{2}{}_0 \mathbf{U}^T \mathbf{N}_{ij}^{(m)}{}_0 \mathbf{U}, \quad (30b)$$

$${}^0\kappa_{ij}^{(m)} = \frac{1}{2}{}_0 \mathbf{U}^T ({}^t\mathbf{g}_j^{(m)} \hat{\mathbf{Q}}_{,i}^{(m)} + {}^t\mathbf{g}_i^{(m)} \hat{\mathbf{Q}}_{,j}^{(m)})_0 \mathbf{U} = \frac{1}{2}{}_0 \mathbf{U}^T \mathbf{N}_{ij}^{(m)}{}_0 \mathbf{U}, \quad (30c)$$

in which

$$\mathbf{L}_{,i}^{(m)} = \frac{\partial \mathbf{L}^{(m)}}{\partial r_i} \quad \text{and} \quad \hat{\mathbf{Q}}_{,i}^{(m)} = \left[\frac{\partial_1 \mathbf{Q}^{(m)}}{\partial r_i} \quad \frac{\partial_2 \mathbf{Q}^{(m)}}{\partial r_i} \quad \frac{\partial_3 \mathbf{Q}^{(m)}}{\partial r_i} \right]^T. \quad (31)$$

Using Eq. (24), the incremental covariant Green–Lagrange strains are transformed into the local Green–Lagrange strains, as follows

$${}^0\bar{e}_{ij}^{(m)} = \mathbf{B}_{ij}^{(m)}(\mathbf{t}_i \cdot \mathbf{g}^{k(m)})(\mathbf{t}_j \cdot \mathbf{g}^{l(m)})_0 \mathbf{U} = \bar{\mathbf{B}}_{ij}^{(m)} {}^0\mathbf{U}, \quad (32a)$$

$${}^0\bar{\eta}_{ij}^{(m)} = \frac{1}{2} {}^0\mathbf{U}^T {}_1\mathbf{N}_{ij}^{(m)}(\mathbf{t}_i \cdot \mathbf{g}^{k(m)})(\mathbf{t}_j \cdot \mathbf{g}^{l(m)})_0 \mathbf{U} = \frac{1}{2} {}^0\mathbf{U}^T {}_1\bar{\mathbf{N}}_{ij}^{(m)} {}^0\mathbf{U}, \quad (32b)$$

$${}^0\bar{\kappa}_{ij}^{(m)} = \frac{1}{2} {}^0\mathbf{U}^T {}_2\mathbf{N}_{ij}^{(m)}(\mathbf{t}_i \cdot \mathbf{g}^{k(m)})(\mathbf{t}_j \cdot \mathbf{g}^{l(m)})_0 \mathbf{U} = \frac{1}{2} {}^0\mathbf{U}^T {}_2\bar{\mathbf{N}}_{ij}^{(m)} {}^0\mathbf{U}, \quad (32c)$$

and their variations are obtained as follows

$$\delta_0 \bar{e}_{ij}^{(m)} = \bar{\mathbf{B}}_{ij}^{(m)} \delta_0 \mathbf{U}, \quad \delta_0 \bar{\eta}_{ij}^{(m)} = \delta_0 \mathbf{U}^T {}_1\bar{\mathbf{N}}_{ij}^{(m)} {}^0\mathbf{U} \quad \text{and} \quad \delta_0 \bar{\kappa}_{ij}^{(m)} = \delta_0 \mathbf{U}^T {}_2\bar{\mathbf{N}}_{ij}^{(m)} {}^0\mathbf{U}. \quad (33)$$

4. Incremental equilibrium equations

The general nonlinear response is calculated using incremental equilibrium equations in which, when the configuration at time t is known, the principle of virtual work in the configuration at time $t + \Delta t$ is considered. Based on the total Lagrangian formulation, the tangent stiffness matrix and internal force vector are derived for the incremental equilibrium equations. A single beam element is considered in this derivation because the incremental equilibrium equations for an entire beam finite element model can be easily constructed using the direct stiffness procedure [1].

The total Lagrangian formulation for the continuum mechanics based beam is given by [1,14,30]

$$\int_{{}^0V} \bar{C}_{ijkl} {}^0\bar{e}_{ij} \delta_0 \bar{e}_{kl} d^0V + \int_{{}^0V} {}^t_0\bar{S}_{ij} \delta_0 \bar{\eta}_{ij} d^0V + \int_{{}^0V} {}^t_0\bar{S}_{ij} \delta_0 \bar{\kappa}_{ij} d^0V = {}^{t+\Delta t}\mathfrak{R} - \int_{{}^0V} {}^t_0\bar{S}_{ij} \delta_0 \bar{e}_{ij} d^0V, \quad (34)$$

in which 0V is the volume of the beam element at time 0, ${}^{t+\Delta t}\mathfrak{R}$ is the external virtual work including the work due to the applied surface tractions and body forces, and \bar{C}_{ijkl} and ${}^t_0\bar{S}_{ij}$ denote the material law tensor and second Piola–Kirchhoff stress measured in the local Cartesian coordinate system, respectively.

As mentioned in the previous section, only five strain components (and corresponding stress components) are considered in the beam formulation (i.e. $(i, j) \in \{(1, 1), (1, 2), (2, 1), (1, 3), (3, 1)\}$) and the material law tensor has only five non-zero components ($\bar{C}_{1111} = E$ and $\bar{C}_{1212} = \bar{C}_{2121} = \bar{C}_{1313} = \bar{C}_{3131} = G$) with Young's modulus E and shear modulus G .

Substituting Eqs. (32a), (32b), (32c), and (33) into Eq. (34), the following discretized equation is obtained

$$\begin{aligned} & \delta_0 \mathbf{U}^T \left[\sum_{m=1}^n \int_{{}^0V^{(m)}} \bar{\mathbf{B}}_{ij}^{(m)T} \bar{C}_{ijkl} \bar{\mathbf{B}}_{kl}^{(m)} dV^{(m)} + \sum_{m=1}^n \int_{{}^0V^{(m)}} {}_1\bar{\mathbf{N}}_{ij}^{(m)T} {}^t_0\bar{S}_{ij} dV^{(m)} + \sum_{m=1}^n \int_{{}^0V^{(m)}} {}_2\bar{\mathbf{N}}_{ij}^{(m)T} {}^t_0\bar{S}_{ij} dV^{(m)} \right] {}^0\mathbf{U} \\ & = \delta_0 \mathbf{U}^T {}^{t+\Delta t}\mathbf{R} - \delta_0 \mathbf{U}^T \left[\sum_{m=1}^n \int_{{}^0V^{(m)}} \bar{\mathbf{B}}_{ij}^{(m)T} {}^t_0\bar{S}_{ij} dV^{(m)} \right], \end{aligned} \quad (35)$$

in which n is the number of sub-beams considered in the continuum mechanics based beam, ${}^0V^{(m)}$ is the volume of the sub-beam m at time 0, and ${}^0V = \sum_{m=1}^n {}^0V^{(m)}$.

Finally, the linearized incremental equilibrium equations are obtained as follows

$${}^t\mathbf{K}_0 \mathbf{U} = {}^{t+\Delta t}\mathbf{R} - {}^t_0\mathbf{F} \quad \text{with} \quad {}^t\mathbf{K} = {}^t\mathbf{K}_L + {}^t_1\mathbf{K}_{NL} + {}^t_2\mathbf{K}_{NL}, \quad (36)$$

in which

$${}^t\mathbf{K}_L = \sum_{m=1}^n \int_{{}^0V^{(m)}} \bar{\mathbf{B}}_{ij}^{(m)T} \bar{C}_{ijkl} \bar{\mathbf{B}}_{kl}^{(m)} dV^{(m)}, \quad (37a)$$

$${}^t_1\mathbf{K}_{NL} = \sum_{m=1}^n \int_{{}^0V^{(m)}} {}_1\bar{\mathbf{N}}_{ij}^{(m)T} {}^t_0\bar{S}_{ij} dV^{(m)}, \quad (37b)$$

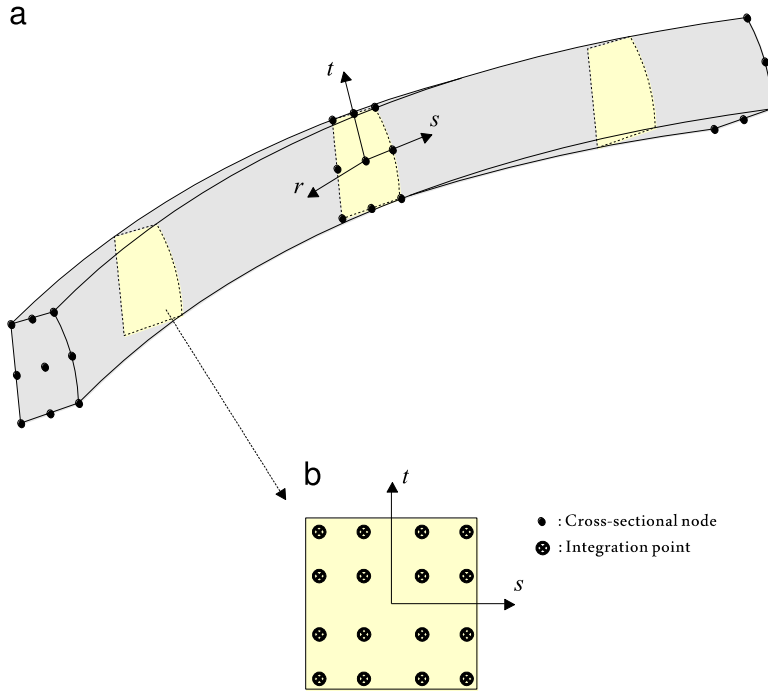


Fig. 3. Gauss integration points in the sub-beam element m in Fig. 1: (a) sub-beam element m and (b) Gauss integration points in beam cross-sections.

$${}^t_2 \mathbf{K}_{NL} = \sum_{m=1}^n \int_{0V^{(m)}} 2 \bar{\mathbf{N}}_{ij}^{(m)t} {}^t_0 \bar{S}_{ij} dV^{(m)}, \quad (37c)$$

$${}^t_0 \mathbf{F} = \sum_{m=1}^n \int_{0V^{(m)}} \bar{\mathbf{B}}_{ij}^{(m)T} {}^t_0 \bar{S}_{ij} dV^{(m)}. \quad (37d)$$

Note that, in Eq. (36), ${}^{t+\Delta t} \mathbf{R}$ is the external load vector and the tangent stiffness matrix ${}^t \mathbf{K}$ is symmetric and complete.

After solving Eq. (36) in each incremental step, the incremental displacement ${}^0 \mathbf{U}$ is obtained. Then, the position of beam node k and the warping degree of freedom at beam node k are additively updated, as follows

$${}^{t+\Delta t}_0 \mathbf{x}_k = {}^t_0 \mathbf{x}_k + \begin{bmatrix} {}^0 u_k \\ {}^0 v_k \\ {}^0 w_k \end{bmatrix}, \quad \text{and} \quad {}^{t+\Delta t}_0 \alpha_k = {}^t_0 \alpha_k + {}^0 \alpha_k, \quad (38)$$

and the director vectors are multiplicatively updated using Eq. (7).

In order to avoid shear and membrane lockings, the well-known assumed strain scheme, namely the MITC (Mixed Interpolation of Tensorial Components) scheme, is adopted [41–45]. Note that, compared with the reduced integration scheme, the MITC scheme enables better performance, particularly for complicated beam geometries. Therefore, the full Gauss integration is used to evaluate the stiffness matrices and internal force vector in Eqs. (37a), (37b), (37c), and (37d). For example, Fig. 3 illustrates the 3, 4, and 4 integration points in the r , s , and t directions, respectively, for the sub-beam element m in Fig. 1. That is, 3 integration points for the longitudinal direction and 4×4 integration points in the sub-beam cross-section are used, which will be referred as $3 \times 4 \times 4$ integration in the following sections.

In order to simulate the material nonlinearity, the three-dimensional von Mises plasticity model with the associated flow rule and linear isotropic hardening in Ref. [46] was implemented. The constitutive equations for the three dimensional beam are derived from the beam state projected von Mises model. At each integration point, the constitutive equations are implicitly solved using the return mapping scheme. Note that, for the material nonlinear analyses, higher order Gauss integrations could be required for better accuracy.

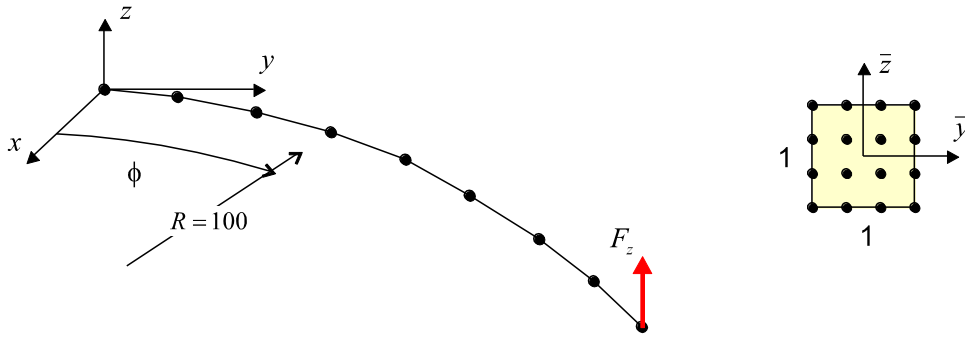


Fig. 4. 45-degree bend beam problem with a square cross-section and its longitudinal and cross-sectional meshes.

5. Numerical examples

In this section, we present several numerical examples to demonstrate the performance and modeling capabilities of the continuum mechanics based beam elements in nonlinear analyses. In this section, 2- and 3-node continuum mechanics based beam elements are considered. The standard full Newton–Raphson iterative scheme is employed for the nonlinear solutions in all examples.

The results obtained using the proposed beam elements are compared with the reference solutions obtained from the beam, solid, and shell elements in ADINA [47] and the beam element in ANSYS (BEAM188) [48]:

- ADINA BEAM: The beam element in ADINA is formulated using the Euler beam theory with Hermitian polynomials. The Wagner strain term is explicitly contained in the beam formulation.
- BEAM188: BEAM188 in ANSYS is based on the Timoshenko beam theory. This beam element does not consider the Wagner strain effect [22].

Note that the large twisting problems considered here are mostly not easy to solve even though very fine solid and shell element models are used; see Table 1 for the large twisting capability of the beam, shell, and solid element models.

5.1. 45-degree bend beam problem

The classical benchmark problem proposed by Bathe and Bolourchi [11] is considered. A 45-degree circular cantilever beam with a radius of $R = 100$ has a square cross-section, as shown in Fig. 4. At $\phi = 0^\circ$, the beam is fully clamped: $u = v = w = \theta_x = \theta_y = \theta_z = \alpha = 0$. The z -directional load $F_z = 600$ is applied at the free tip ($\phi = 45^\circ$). The linear elastic material with Young's modulus $E = 1.0 \times 10^7$ and Poisson's ratio $\nu = 0$ is used. The beam is modeled using eight 2-node continuum mechanics based beam elements and the cross-section is discretized using one 16-node cubic cross-sectional element.

Fig. 5 illustrates the load–displacement curves calculated using the 2-node continuum mechanics based beams, and the results are compared with the reference solutions obtained from eight ADINA BEAMs with 20 incremental load steps. The present beam element provides good agreement even when only two incremental load steps are used. Table 2 lists the free tip displacements calculated using the 2- and 3-node continuum mechanics based beam elements compared with various previous results [11,13,14,33,39,40,49,50].

5.2. Z-shaped cross-section beam problem

We consider the benchmark problem proposed by Wackerfuß and Gruttmann [29]. As shown in Fig. 6, a straight cantilever beam of $L = 1$ m is considered with a Z-shaped cross-section. The beam is modeled using two 2-node continuum mechanics based beam elements and the cross-section is discretized using seven 16-node cubic cross-sectional elements. The boundary condition $u = v = w = \theta_x = \theta_y = \theta_z = \alpha = 0$ is applied at $x = 0$ m. The twist angle θ_x is prescribed at the free tip ($x = 1$ m). The elastic–perfectly-plastic material ($E = 2.1 \times 10^{11}$ N/m², $\nu = 0.3$, and yield stress $Y_0 = 2.4 \times 10^5$ kN/m²) is used.

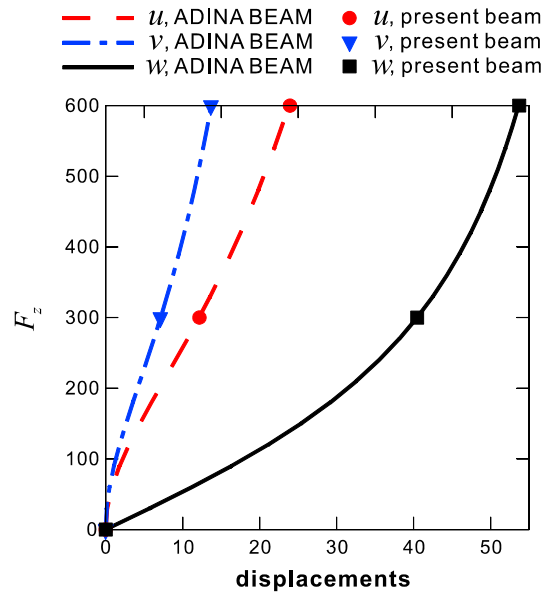


Fig. 5. Load–displacement curves at the free tip in the 45-degree bend beam problem.

Table 1

Large twisting analysis capability of the beam, shell, and solid element models in the numerical examples considered in this study (○: capable, X: incapable).

| Beam problems | Solid element model (ADINA) | Shell element model (ADINA) | Beam element models | | |
|--|--------------------------------|--------------------------------|-----------------------|--------------------|--------------|
| | | | ADINA BEAM (ADINA) | BEAM188 (ANSYS) | Present beam |
| Cross-shaped cross-section beam problem (Section 5.3, Load Case II) | ○ | X | X | X | ○ |
| Twisted cantilever beam problem (Section 5.4, Load Case I) | ○ | ○ | X | X | ○ |
| Twisted cantilever beam problem (Section 5.4, Load Case II) | ○ | ○ | X | X | ○ |
| Twisted cantilever beam problem (Section 5.4, Load Case III) | X | X | X | X | ○ |
| Lateral post-buckling problem (Section 5.5) | ○ | ○ | ○ | X | ○ |

Table 2

Free tip displacements when $F_z = 600$ N in the 45-degree bend beam problem.

| | Displacements | | |
|--------------------------------------|---------------|---------|--------|
| | u | v | w |
| Bathe and Bolourchi [11] | −13.4 | −23.5 | 53.4 |
| Simo and Vu-Quoc [49] | −13.49 | −23.48 | 53.37 |
| Dvorkin et al. [14] | −13.6 | −23.5 | 53.3 |
| Cardona and Geradin [13] | −13.74 | −23.67 | 53.5 |
| Ibrahimbegović et al. [39] | −13.668 | −23.697 | 53.498 |
| Jelenić and Crisfield [50] | −13.483 | −23.479 | 53.371 |
| Schulz and Filippou [33] | −13.53 | −23.46 | 53.37 |
| Ritto-Corrêa and Camotim [40] | −13.668 | −23.696 | 53.498 |
| Eight 2-node beam elements (present) | −13.659 | −23.938 | 53.711 |
| Four 3-node beam elements (present) | −13.729 | −23.821 | 53.615 |

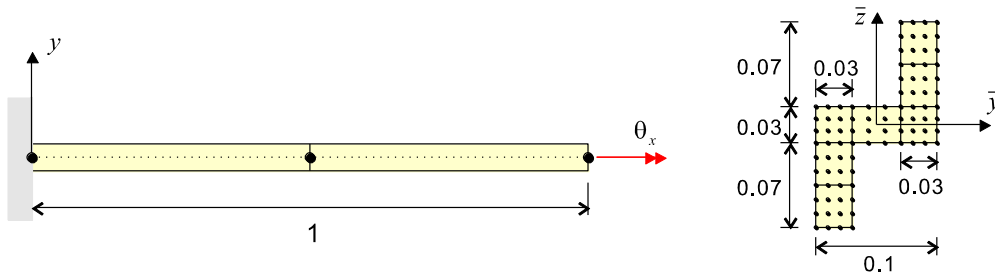


Fig. 6. Z-shaped cross-section beam problem and its longitudinal and cross-sectional meshes (unit: m).

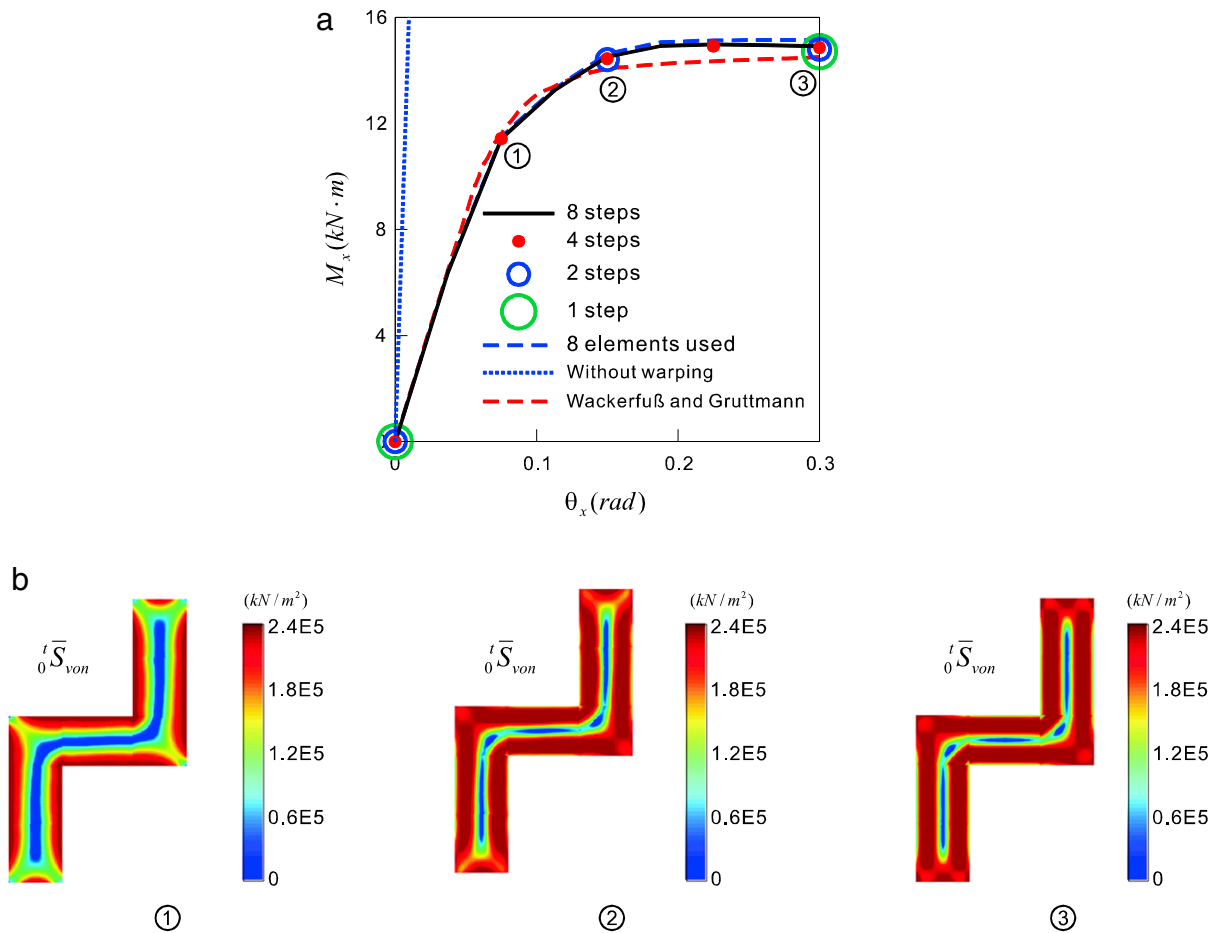


Fig. 7. Numerical results in the Z-shaped cross-section beam problem: (a) load–displacement curves and (b) distributions of the von Mises stress obtained from the continuum mechanics based beam elements.

Fig. 7(a) displays the load–displacement curves calculated using two 2-node beam elements with four different incremental steps (1, 2, 4, and 8 incremental steps) and using eight 2-node beam elements with 8 incremental steps. The numerical results are in good agreement with the reference solution obtained by Wackerfuß and Gruttmann [29]. The almost full plastic state is reached with only a single incremental step. Fig. 7(b) illustrates the von Mises stress distributions on the cross-section at $x = 0.5$ m obtained from the continuum mechanics based beam elements. The propagation of the yield region is observed.

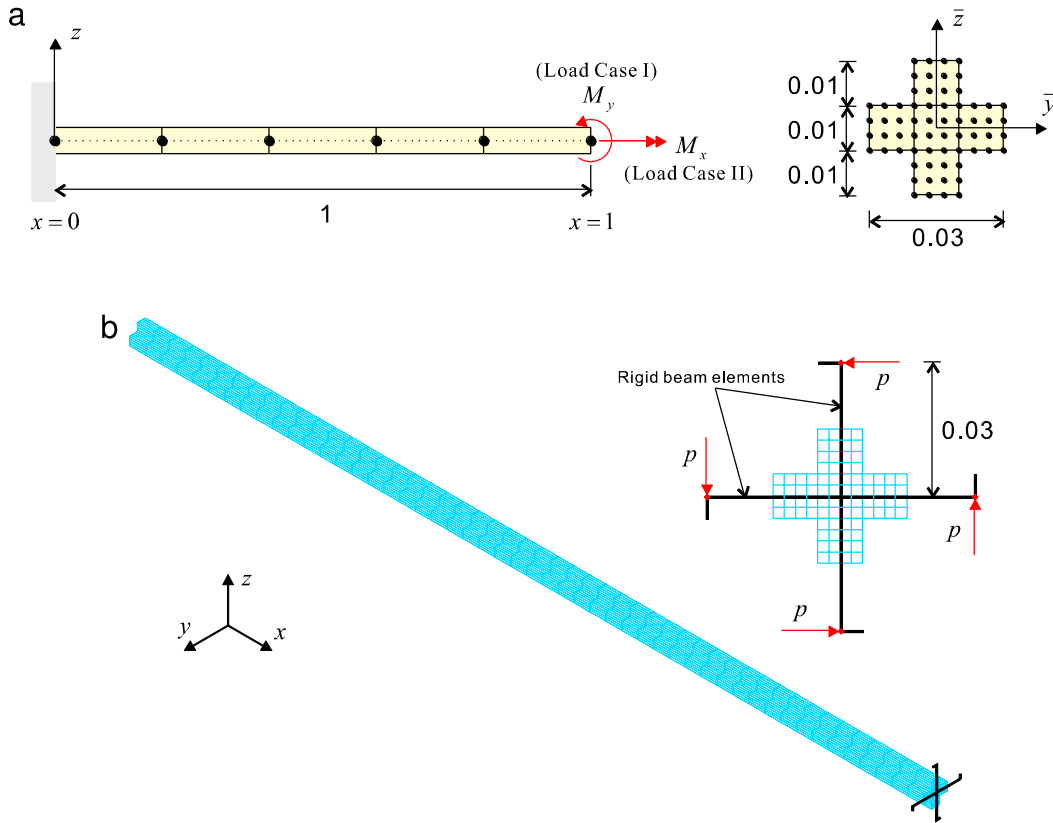


Fig. 8. Cross-shaped cross-section beam problem (unit: m): (a) longitudinal and cross-sectional meshes used in the beam model (5 beam elements) and (b) solid element model used (4000 solid elements).

5.3. Cross-shaped cross-section beam problem

We consider a straight cantilever beam with a length of $L = 1$ m and a cross-shaped cross-section, as shown in Fig. 8(a). The beam is modeled using five continuum mechanics based beam elements and the cross-section is discretized using five 16-node cubic cross-sectional elements. The boundary condition $u = v = w = \theta_x = \theta_y = \theta_z = \alpha = 0$ is applied at $x = 0$ m. Two load cases are considered:

- Load Case I: The bending moment M_y is applied at the free tip ($x = 1$ m).
- Load Case II: The twisting moment (torsion) M_x is applied at the free tip ($x = 1$ m).

To obtain the reference solution for Load Case II, four thousand 27-node solid elements are used in the solid element model presented in Fig. 8(b). In order to appropriately apply the twisting moment in the cross-section at the free tip, four rigid beam elements are also modeled and four point loads $p = M_x / (4 \times 0.03)$ are applied at the end tip of each rigid beam element, as seen in Fig. 8(b). All degrees of freedom are fixed at $x = 0$ m.

Fig. 9 presents the responses calculated for Load Case I with the linear elastic material (Young's modulus $E = 2.0 \times 10^{11}$ N/m² and Poisson's ratio $\nu = 0$). Fig. 9(a) illustrates the load–displacement curves calculated using five 2-node beam elements with four different load steps (2, 4, 8, and 16 load steps), and Fig. 9(b) shows the corresponding deformed shapes. The tip rotation 2π can be reached using only two load steps. Fig. 9(c) shows the load–displacement curves obtained from five 3-node beam elements with three different load steps (6, 12, and 24 load steps), and the corresponding deformed shapes are presented in Fig. 9(d). The tip rotation 4π can be calculated using only 6 load steps.

Fig. 10 shows the responses obtained for Load Case II when the elastic–perfectly-plastic material ($E = 2.0 \times 10^{11}$ N/m², $\nu = 0$, and yield stress $Y_0 = 1.0 \times 10^6$ kN/m²) is used. Fig. 10(a) presents the load–displacement curves calculated using five 2-node beam elements (42 DOFs) with four different load steps (1, 2, 4, and 8 load steps). The almost full plastic state is reached with only a single load step. The reference solutions are obtained using

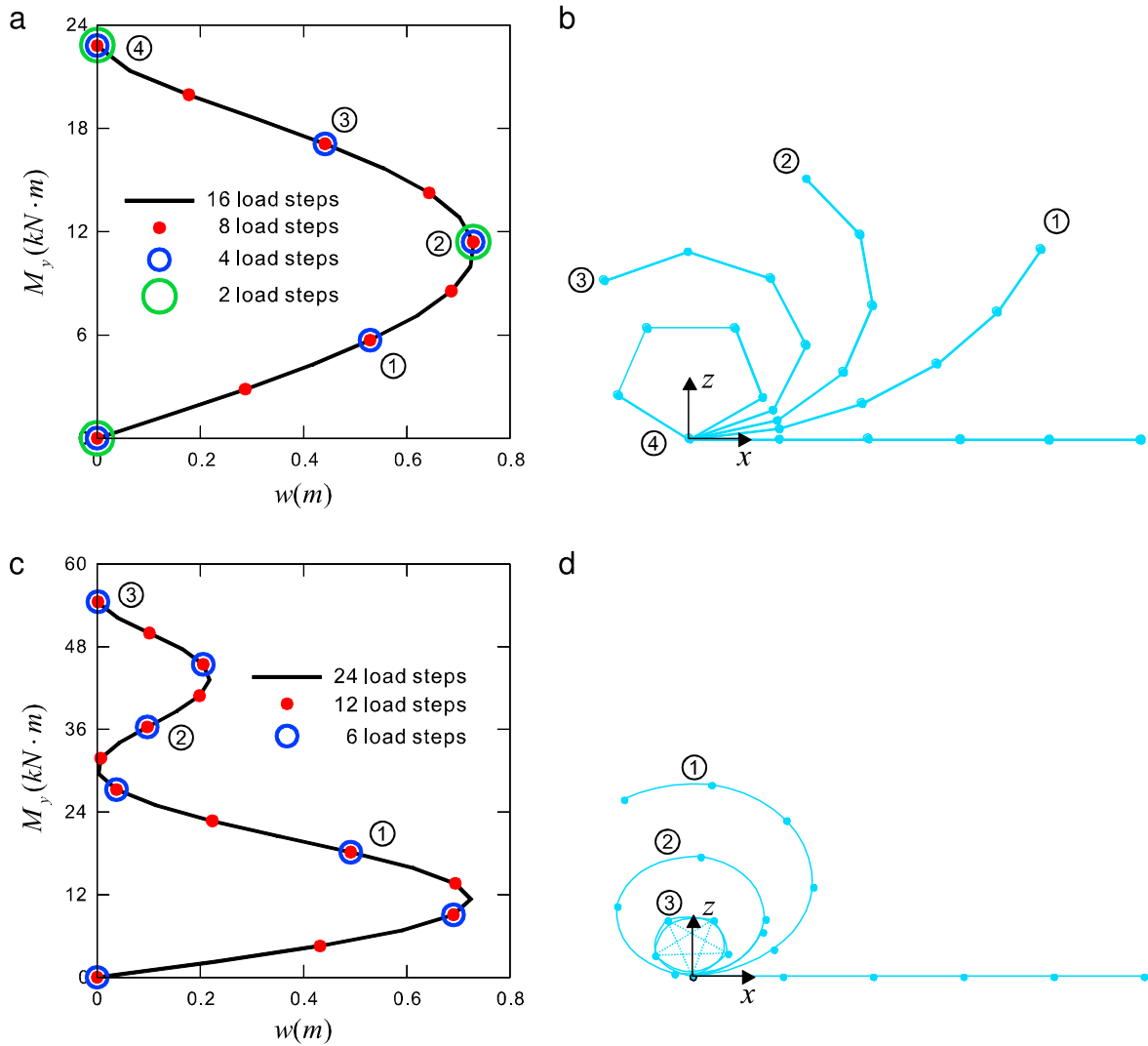


Fig. 9. Numerical results for Load Case I in the cross-shaped cross-section beam problem: (a) and (b) load-displacement curves and deformed shapes, respectively, when five 2-node beam elements were used; and (c) and (d) load-displacement curves and deformed shapes, respectively, when five 3-node beam elements used. (Note: The center nodes of the 3-node beam elements are not plotted.)

four thousand 27-node solid elements (111,894 DOFs) with 800 load steps using ADINA. In the calculation of the reference solutions, the plastic response cannot be captured with 400 load steps, and the analysis with 800 load steps is also terminated early, as seen in Fig. 10(a). Figs. 10(b) and (c) display the von Mises stress distributions on the cross-section at $x = 0.5$ m in the beam and solid element models, respectively. It is observed that the yield region is propagating appropriately in the beam element model.

5.4. Twisted cantilever beam problem

Consider the twisted cantilever beam with a thin rectangular cross-section as illustrated in Fig. 11(a). The beam length is 2 m and the total twisted angle is 2π . The boundary condition $u = v = w = \theta_x = \theta_y = \theta_z = \alpha = 0$ is applied at $x = 0$ m. The linear elastic material with Young's modulus $E = 2.0 \times 10^{11}$ N/m² and Poisson's ratio $\nu = 0$ is used. The following three load cases are considered:

- Load Case I: The shear force F_y is applied at the free tip ($x = 2$ m).
- Load Case II: The displacement u is prescribed at the free tip ($x = 2$ m).

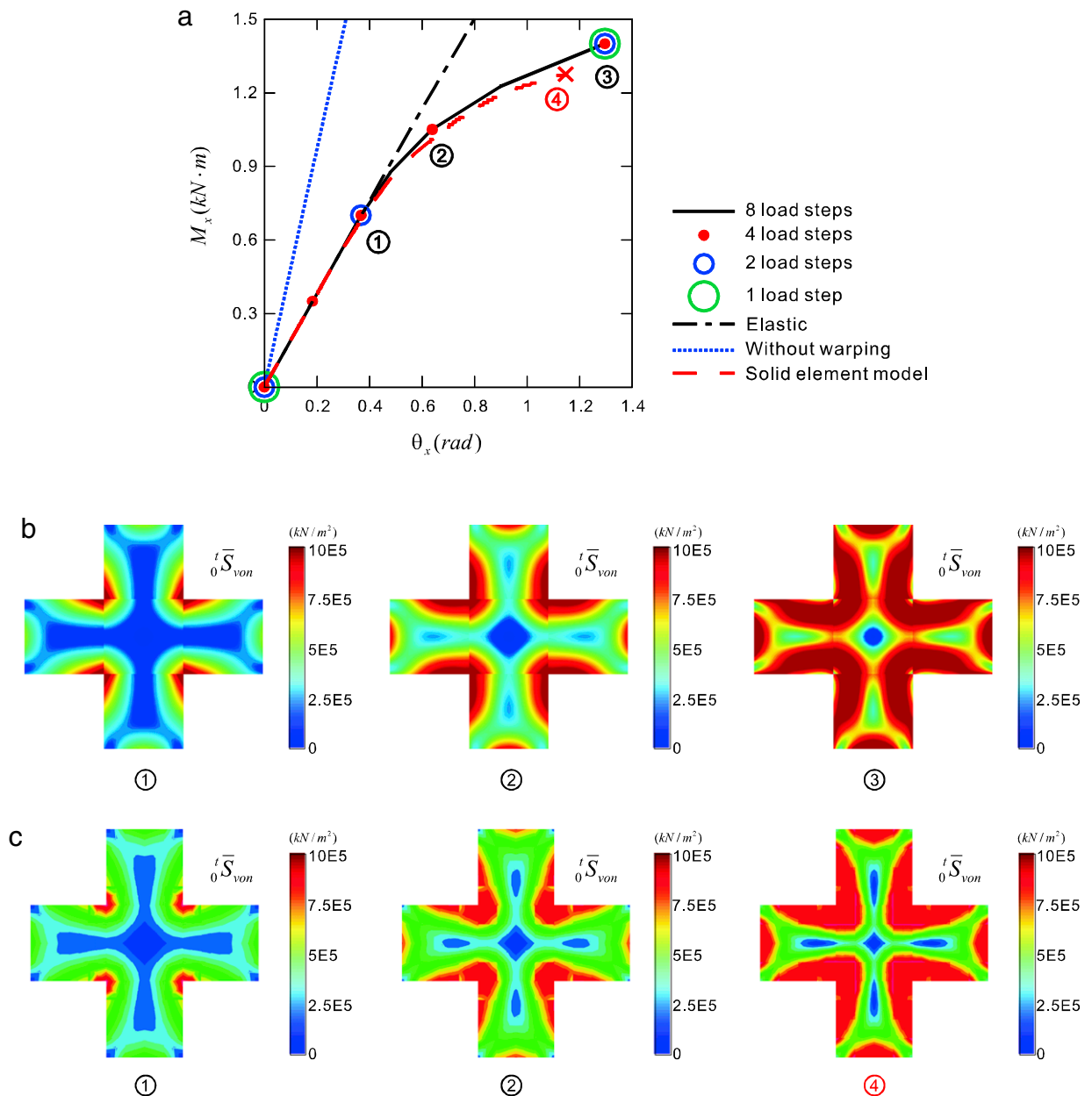


Fig. 10. Numerical results for Load Case II in the cross-shaped cross-section beam problem (five 2-node beam elements): (a) load–displacement curves, (b) distributions of the von Mises stress obtained from the beam element model, and (c) distributions of the von Mises stress obtained from the solid element model.

- Load Case III: The twist angle θ_x is prescribed at the free tip ($x = 2$ m).

The twisted cantilever beam is modeled using eight 2-node beam elements, and the thin rectangular cross-section is discretized using one 4-node cross-sectional element, as seen in Fig. 11(b). In order to consider the twisted geometry, the director vectors are initially given as described in Fig. 11(b).

In order to obtain the reference solutions, the MITC4 shell elements (800 elements) are used in the shell element model presented in Fig. 11(c). Two point loads $p = 0.5F_y$ are applied at $x = 2$ m for Load Case I, and the prescribed displacement u is applied to all nodes at $x = 2$ m for Load Case II. All degrees of freedom are fixed at $x = 0$ m.

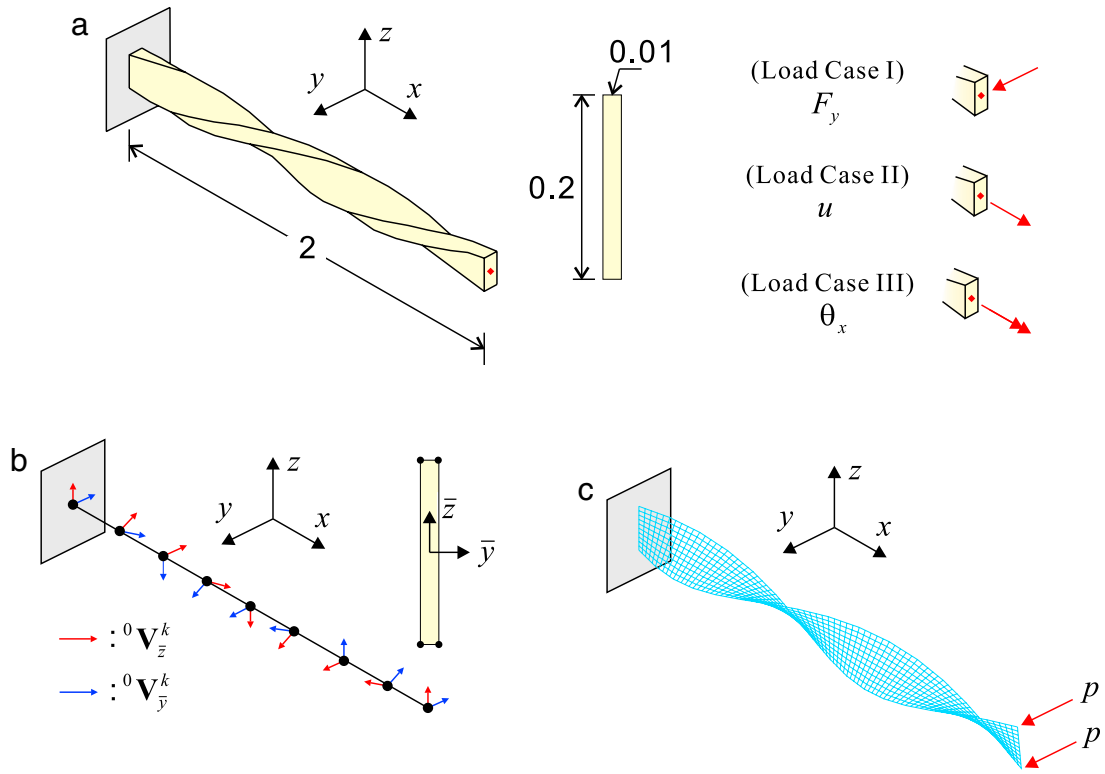


Fig. 11. Twisted cantilever beam problem (unit: m): (a) problem description and (b) the longitudinal and cross-sectional meshes used (8 beam elements). The twisted geometry is modeled simply through changing the director vectors of the continuum mechanics based beams (${}^0\mathbf{V}_{\bar{y}}^k$ and ${}^0\mathbf{V}_{\bar{z}}^k$). (c) Shell element model (800 shell elements).

Figs. 12(a) and (b) display the load–displacement curves for Load Case I and the twist angle–stretch relation for Load Case II. For Load Case II, Figs. 13(a) and (b) show the deformed shapes obtained from the shell element model and beam element model, respectively. The numerical results of the beam element model exhibit good agreement with the reference shell solutions. Note that, in order to obtain appropriate responses in this beam problem, the coupled behavior of stretching, bending, shearing, twisting, and warping should be correctly considered in the beam formulation.

For Load Case III, Figs. 14(a) and (b) present the torsional moment M_x and longitudinal displacement u at the free tip according to the twist angle at the free tip. The corresponding deformed shapes are plotted in Fig. 14(c). As the twist angle increases, the twisted beam is unwound from $\theta_x = 0$ to 2π , and then it is rewound from $\theta_x = 2\pi$ to 4π . It is very interesting to observe the snap through phenomenon in Fig. 14(a), and the lengthening and shortening due to the unwinding and rewinding in Fig. 14(b). Note that Load Case III cannot be analyzed using the solid and shell element models due to convergence problems. Further studies are required for understanding the numerical difficulty as well as the physical phenomenon.

5.5. Lateral post-buckling problem

Through lateral post-buckling analyses, this section demonstrates how well the present beam element captures the Wagner effect. As illustrated in Fig. 15(a), a straight cantilever beam of $L = 1651$ mm is considered with a mono-symmetric I-section, which was used in the lateral post-buckling experiment conducted by Anderson and Trahair [51]. Young's modulus E is 65.123×10^3 N/mm² and shear modulus G is 25.967×10^3 N/mm².

The boundary condition $u = v = w = \theta_x = \theta_y = \theta_z = \alpha = 0$ is applied at $x = 0$ mm and the following four load cases are considered, see Fig. 15(b):

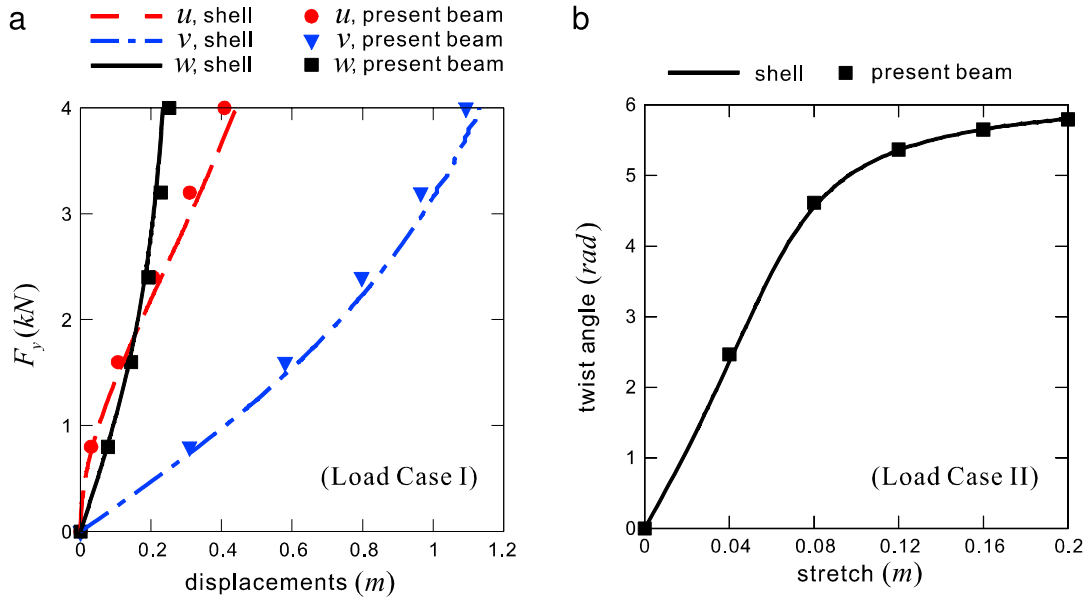


Fig. 12. Numerical results in the twisted cantilever beam problem: (a) load-displacement curves at the free tip for Load Case I and (b) twist angle-stretch relationship for Load Case II when the prescribed displacement is applied.

- Load Case I: The upward direction load is applied at the upper flange at the free tip.
- Load Case II: The downward direction load is applied at the upper flange at the free tip.
- Load Case III: The upward direction load is applied at the lower flange at the free tip.
- Load Case IV: The downward direction load is applied at the lower flange at the free tip.

The loads are applied with the y -directional eccentricity of $e = 0.1$ mm for the consideration of imperfections.

The cantilever beam is modeled using eight 2-node beam elements and the mono-symmetric I-section is discretized using seven 16-node cubic cross-sectional elements as shown in Fig. 15(a). For each sub-beam element, $2 \times 4 \times 4$ integration is used. In order to obtain the reference solutions, the MITC4 shell elements (180 elements) are used in the shell element model, as shown in Fig. 15(c). In order to consider the load position and eccentricity, the rigid beam finite elements with a length of 0.1 mm are inserted at the loaded tip. All degrees of freedom are fixed at $x = 0$ mm.

Figs. 16(a) and (b) show the lateral post-buckling responses of the cantilever beam calculated for the four different load cases. Different bifurcation points are observed depending on the direction and position of the load application. To predict this interesting phenomenon accurately, it is important to include the Wagner strain in the beam formulation. Note that, in the present beam formulation, the Wagner strain is automatically considered without pre-calculating Wagner's coefficient and the buckling modes. The bifurcation points and load-displacement curves calculated using the continuum mechanics based beam elements are in good agreement with the experimental results and reference shell solutions.

For comparison, the same mesh is used for the calculations using ADINA BEAM and BEAM188. Since ADINA BEAM cannot consider the load position and eccentricity, rigid beam elements are additionally used at the loaded tip to model the eccentricity. ADINA BEAM captures the complicated bifurcations with acceptable accuracy but, as mentioned, additional modeling effort is necessary. BEAM188 in ANSYS cannot capture these complicated phenomena. Furthermore, Figs. 16(c) and (d) present the lateral post-buckling behaviors when elastoplastic material is used (Young's modulus $E = 65.123 \times 10^3$ N/mm², shear modulus $G = 25.967 \times 10^3$ N/mm², initial yield stress $Y_0 = 40$ N/mm², and hardening modulus $H = 0.5E$).

5.6. Framed dome problem

Finally, a framed dome structure that consists of 18 beam members of a rectangular cross-section is considered as described in Fig. 17 [23,52]. The boundary condition $u = v = w = \theta_x = \theta_y = \theta_z = \alpha = 0$ is applied at nodes on

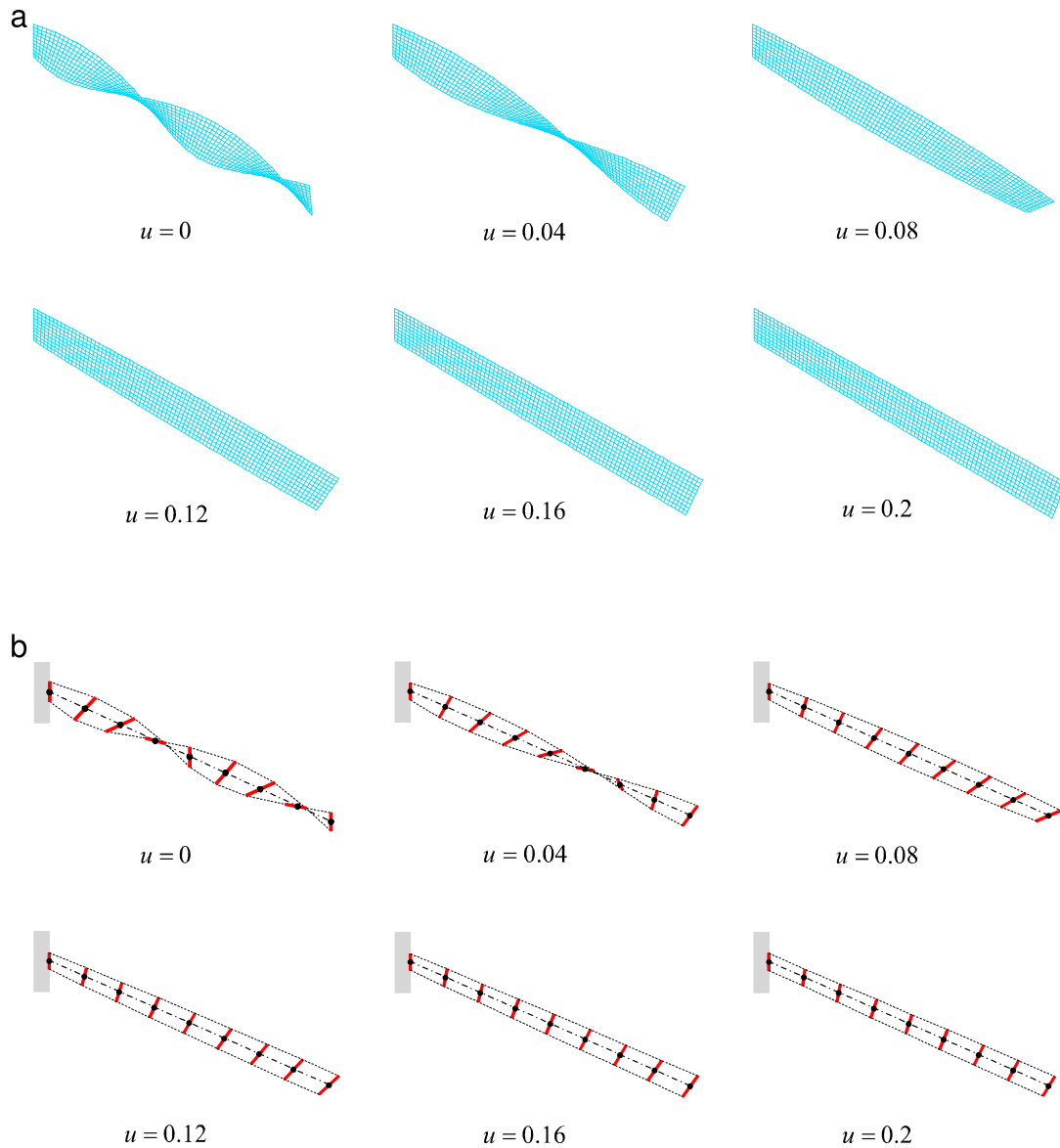


Fig. 13. Deformed shapes for Load Case II in the twisted cantilever beam problem: (a) shell element model and (b) beam element model.

the gray colored areas in Fig. 17. The z -directional concentrate load F_z is applied at the top of the dome. We perform large displacement elastic and elastoplastic analyses. For the elastic analysis, Young's modulus $E = 20690$ and shear modulus $G = 8830$ are used. For the elastoplastic analyses, Young's modulus $E = 20690$, shear modulus $G = 8830$, initial yield stress $Y_0 = 60$, and hardening modulus $H = 0.25E$ are considered. Each beam member is modeled using four 2-node beam elements and the rectangular cross-section is discretized using one 16-node cubic cross-sectional element. The $2 \times 4 \times 4$ integration is used for each beam.

Figs. 18(a) and (b) illustrate the load–displacement curves calculated through incrementally controlling the vertical displacement δ with the elastic and elastoplastic materials. Fig. 18(c) shows the deformed shapes obtained from the elastic analysis. The numerical results are in good agreement with those obtained by Battini [52] and Wackerfuß and Gruttmann [23].

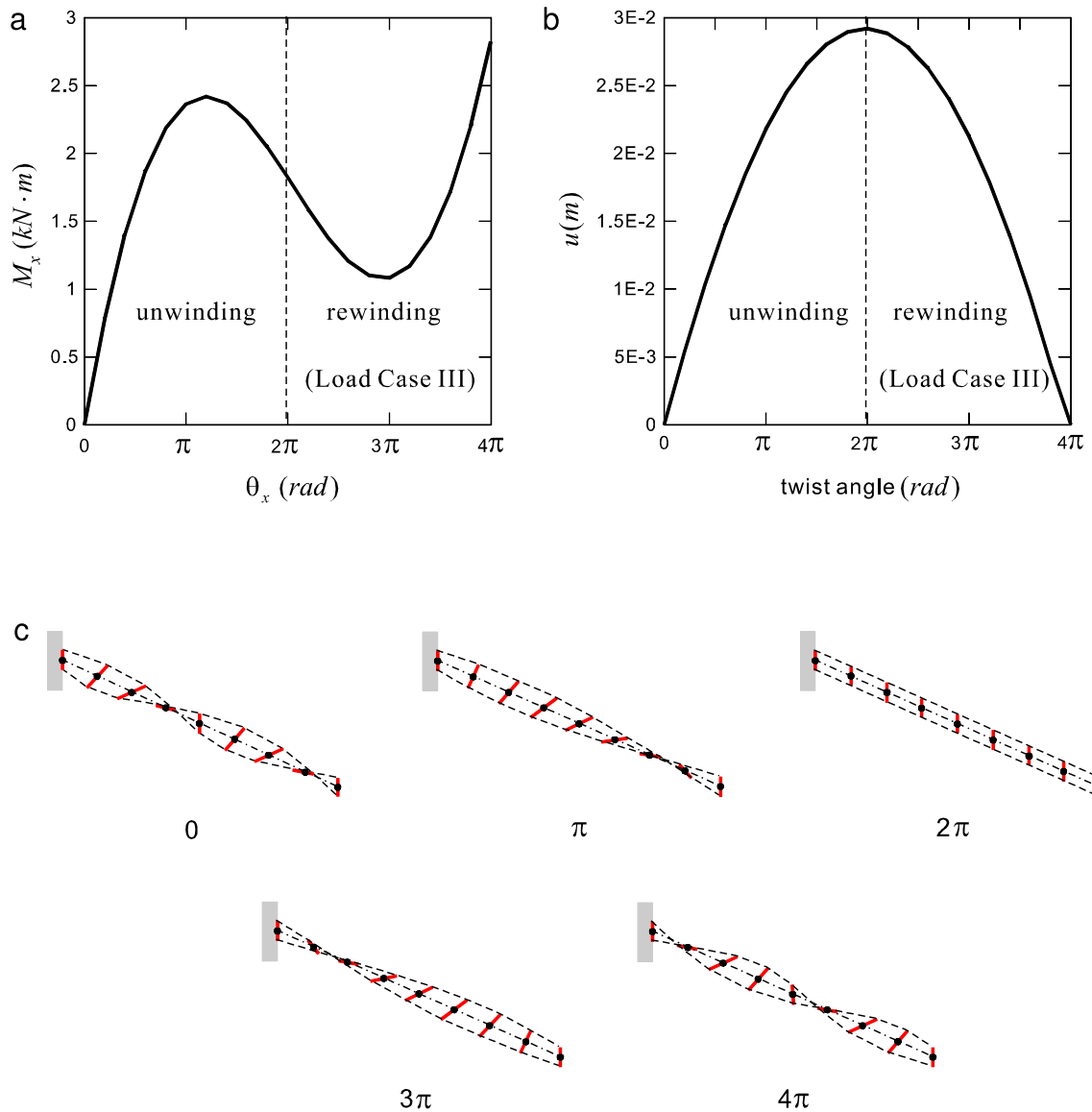


Fig. 14. Numerical results for Load Case III in the twisted cantilever beam problem: (a) load–displacement curve between M_x and θ_x at the free tip, (b) relationship between u and θ_x at the free tip, and (c) deformed shapes when the twist angles at the free tip are 0, π , 2π , 3π , and 4π .

6. Conclusions

In this paper, a nonlinear formulation of the continuum mechanics based beam elements was presented and their performance in general nonlinear analyses that focused on large twisting behaviors was demonstrated. Since the beam elements are derived from assemblages of 3D solid elements, they have inherently advanced modeling capabilities in the analysis of complicated 3D beam geometries including curved and twisted geometries, varying cross-sections, eccentricity, and arbitrary cross-sectional shapes [35,36]. The total Lagrangian formulation was used to obtain the complete tangent stiffness matrix and internal load vector with the warping displacements.

The resulting formulation can consider the fully coupled nonlinear behaviors of bending, shearing, stretching, twisting, and warping. In particular, large twisting and lateral buckling behaviors can be accurately predicted and, in the beam formulation, the Wagner effect is implicitly included, unlike other beam elements. Through various numerical examples, the strong modeling and predictive capabilities of the nonlinear formulation of the continuum mechanics

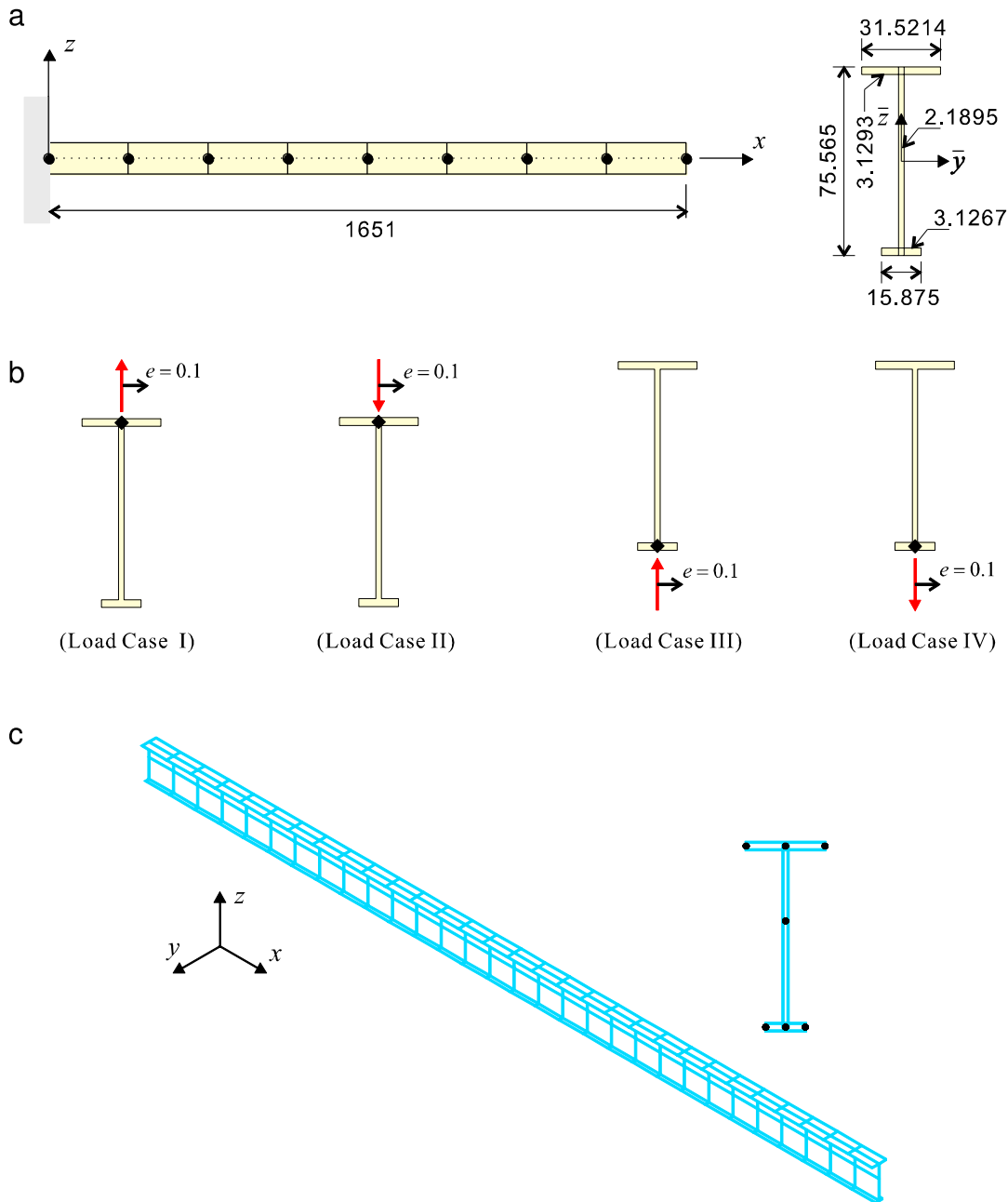


Fig. 15. Lateral post-buckling analyses of a straight cantilever beam with a mono-symmetric I-section (unit: mm): (a) the longitudinal and cross-sectional meshes used (8 beam elements), (b) four load cases, and (c) shell element model (180 shell elements).

based beam elements were demonstrated for general nonlinear analysis. The most valuable asset of the proposed beam elements is their excellent analysis capability in large twisting problems.

Acknowledgments

This work was supported by the Basic Science Research Program through the National Research Foundation of Korea (NRF) funded by the Ministry of Education, Science and Technology (No. 2014R1A1A1A05007219). This work was also conducted under the framework of Research and Development Program of the Korea Institute of Energy Research (KIER) (B4-2453).

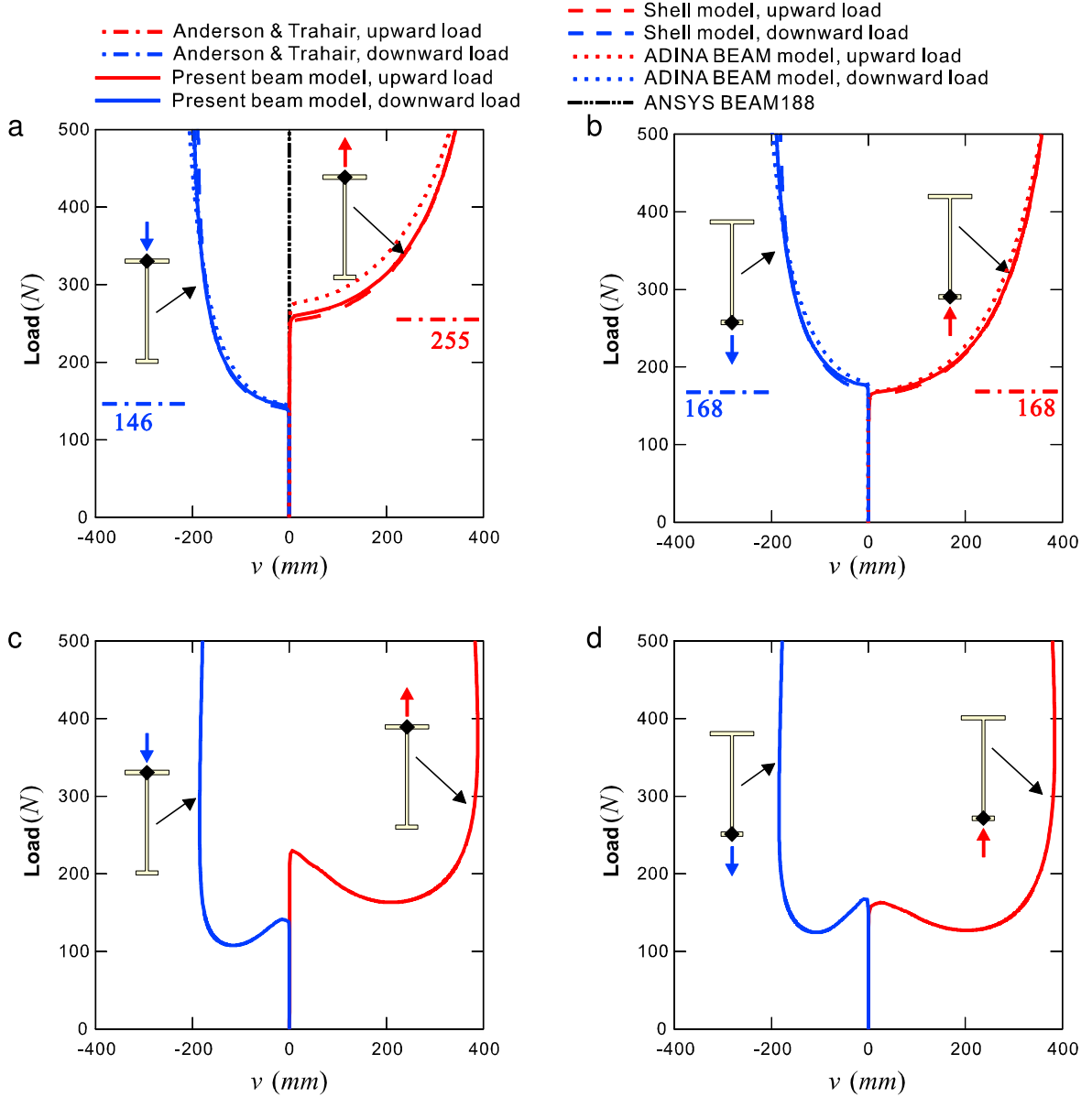


Fig. 16. Lateral post-buckling responses for the four load cases in Fig. 15(b): (a) and (b) elastic material used, and (c) and (d) elastoplastic material used.

Appendix. Wagner strain under pure torsion

The Wagner strain is implicitly included in the geometric nonlinear formulation of the continuum mechanics based beam elements. In order to verify this, the Green–Lagrange strain in the beam formulation is analytically investigated. Two configurations of a rectangular prismatic beam with free warping at time 0 and t are considered: see Fig. 19. Time 0 and t correspond to undeformed and twisted configurations, respectively. The material position vector can be rewritten in the following continuum form (non-discretized form) through deduction from Eq. (1), as follows

$${}^t\mathbf{x} = {}^t\mathbf{x}_r + \bar{y}^t\mathbf{V}_{\bar{y}} + \bar{z}^t\mathbf{V}_{\bar{z}} + {}^t f^t\mathbf{V}_{\bar{x}}, \quad (\text{A.1})$$

in which ${}^t\mathbf{x}_r$ is the position of the beam reference line at time t , ${}^t\mathbf{V}_{\bar{x}}$, ${}^t\mathbf{V}_{\bar{y}}$, and ${}^t\mathbf{V}_{\bar{z}}$ are the director vectors, \bar{y} and \bar{z} denote the position in the cross-sectional plane, and ${}^t f$ is the warping displacement.

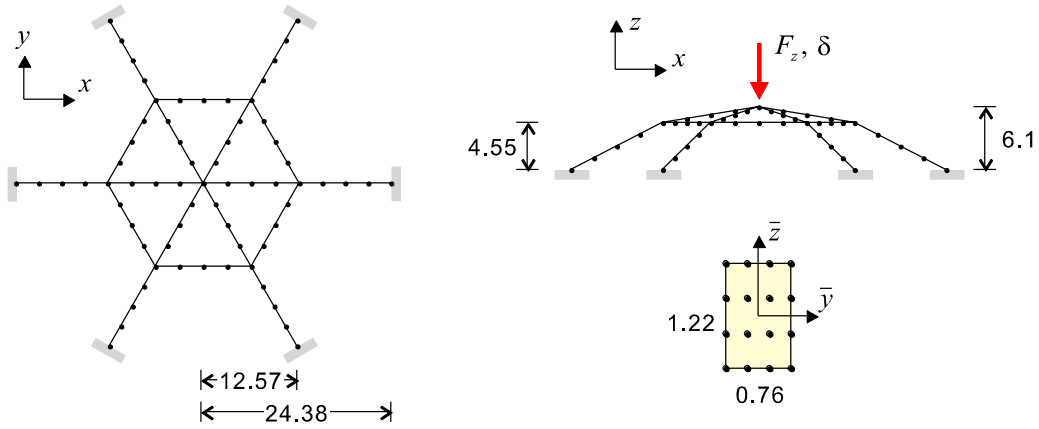


Fig. 17. Framed dome problem and the finite element discretization using the continuum mechanics based beam elements.

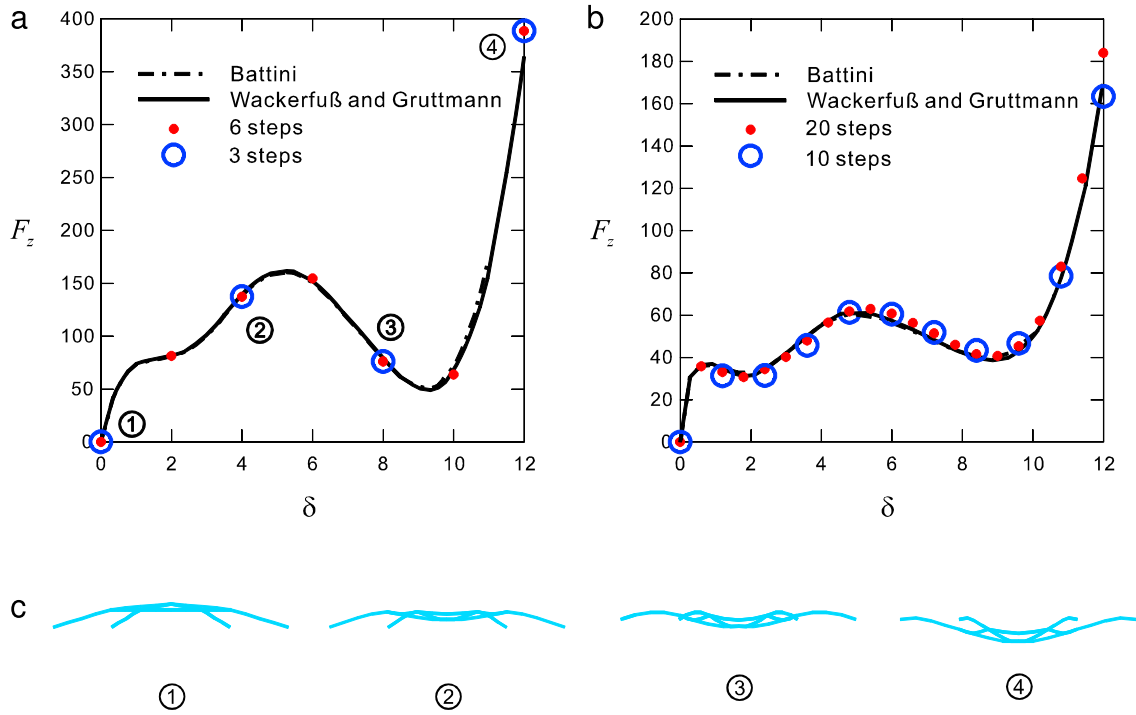


Fig. 18. Numerical results of the framed dome problem: (a) load–displacement curves for the elastic analysis, (b) load–displacement curve for the elastoplastic analysis, and (c) deformed shapes.

Both configurations in Fig. 17 are defined using the following vectors

$${}^0\mathbf{x}_r = {}^t\mathbf{x}_r = \begin{bmatrix} x \\ 0 \\ 0 \end{bmatrix}, \quad {}^0\mathbf{V}_{\bar{x}} = {}^t\mathbf{V}_{\bar{x}} = \begin{bmatrix} 1 \\ 0 \\ 0 \end{bmatrix}, \quad {}^0\mathbf{V}_{\bar{y}} = \begin{bmatrix} 0 \\ 1 \\ 0 \end{bmatrix}, \quad {}^0\mathbf{V}_{\bar{z}} = \begin{bmatrix} 0 \\ 0 \\ 1 \end{bmatrix}, \quad {}^t\mathbf{V}_{\bar{y}} = \begin{bmatrix} 0 \\ \cos \theta_x \\ \sin \theta_x \end{bmatrix},$$

and

$${}^t\mathbf{V}_{\bar{z}} = \begin{bmatrix} 0 \\ -\sin \theta_x \\ \cos \theta_x \end{bmatrix}. \quad (\text{A.2})$$

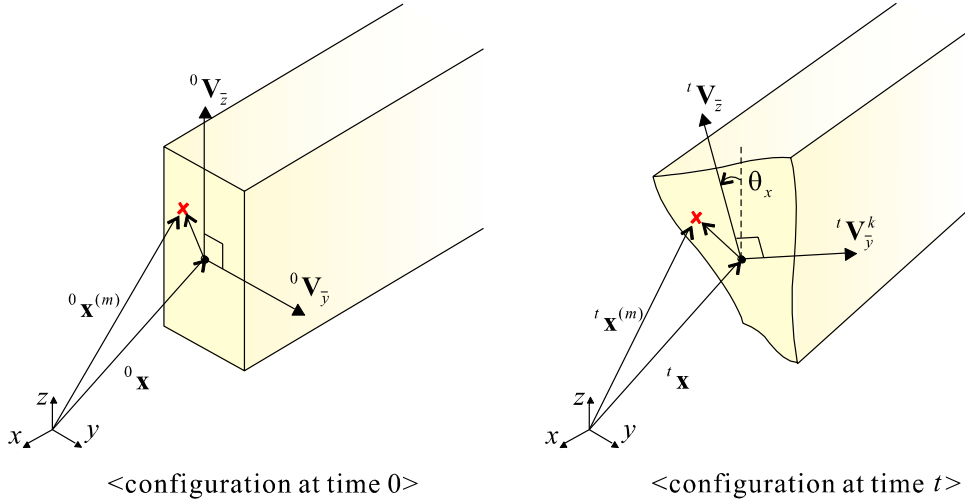


Fig. 19. Initial and deformed configurations of a prismatic straight beam.

Using Eq. (A.2) in Eq. (A.1), the material position vectors at time 0 and t are obtained

$${}^0\mathbf{x} = \begin{bmatrix} x \\ \bar{y} \\ \bar{z} \end{bmatrix} \quad \text{and} \quad {}^t\mathbf{x} = \begin{bmatrix} x + {}^tf \\ \bar{y} \cos \theta_x - \bar{z} \sin \theta_x \\ \bar{y} \sin \theta_x + \bar{z} \cos \theta_x \end{bmatrix}. \quad (\text{A.3})$$

Substituting Eq. (A.3) into Eq. (23), the covariant base vectors (${}^0\mathbf{g}_1$ and ${}^t\mathbf{g}_1$) are obtained

$${}^0\mathbf{g}_1 = \begin{bmatrix} \partial x / \partial r \\ 0 \\ 0 \end{bmatrix} \quad \text{and} \quad {}^t\mathbf{g}_1 = \begin{bmatrix} \partial x / \partial r + \partial {}^tf / \partial r \\ \partial \theta_x / \partial r (-\bar{y} \sin \theta_x - \bar{z} \cos \theta_x) \\ \partial \theta_x / \partial r (\bar{y} \cos \theta_x - \bar{z} \sin \theta_x) \end{bmatrix}, \quad (\text{A.4})$$

and the covariant Green–Lagrange strain ${}^t_0\varepsilon_{11}$ in the configuration at time t , referred to the configuration at time 0, is calculated

$${}^t_0\varepsilon_{11} = \frac{\partial x}{\partial r} \frac{\partial {}^tf}{\partial r} + \frac{1}{2} \left(\frac{\partial {}^tf}{\partial r} \right)^2 + \frac{1}{2} (\bar{y}^2 + \bar{z}^2) \left(\frac{\partial \theta_x}{\partial r} \right)^2. \quad (\text{A.5})$$

Using Eq. (24), the local Green–Lagrange strain ${}^t_0\bar{\varepsilon}_{11}$ is given as follows:

$${}^t_0\bar{\varepsilon}_{11} = \frac{\partial {}^tf}{\partial x} + \frac{1}{2} \left(\frac{\partial {}^tf}{\partial x} \right)^2 + \frac{1}{2} (\bar{y}^2 + \bar{z}^2) \left(\frac{\partial \theta_x}{\partial x} \right)^2. \quad (\text{A.6})$$

In Eq. (A.6), it is easily identified that the Green–Lagrange strain used for the continuum mechanics based beam elements automatically contains the Wagner strain term $1/2(\bar{y}^2 + \bar{z}^2)(\partial \theta_x / \partial x)^2$.

References

- [1] K.J. Bathe, Finite Element Procedures, Prentice Hall, 1996.
- [2] S.P. Timoshenko, J.N. Goodier, Theory of Elasticity, McGraw Hill, 1970.
- [3] V.Z. Vlasov, Thin-Walled Elastic Beams, Israel Program for Scientific Translations, Jerusalem, 1961.
- [4] P.S. Lee, G. McClure, Elastoplastic large deformation analysis of a lattice steel tower structure and comparison with full-scale tests, J. Constr. Steel Res. 63 (2007) 709–717.
- [5] A.G. Neto, C.A. Martins, P.M. Pimenta, Static analysis of offshore risers with a geometrically-exact 3D beam model subjected to unilateral contact, Comput. Mech. 53 (2014) 125–145.
- [6] D.N. Kim, F. Kilchherr, H. Dietz, M. Bathe, Quantitative prediction of 3D solution shape and flexibility of nucleic acid nanostructures, Nucleic Acids Res. 40 (2012) 2862–2868.

- [7] M. Bathe, A finite element framework for computation of protein normal modes and mechanical response, *Proteins: Struct. Funct. Bioinform.* 70 (2008) 1595–1609.
- [8] A. Kumar, S. Mukherjee, J.T. Paci, K. Chandraseker, A rod model for three dimensional deformations of single-walled carbon nanotubes, *Int. J. Solids Struct.* 48 (2011) 2849–2858.
- [9] J. Argyris, P.C. Dunne, D.W. Scarpf, On large displacement-small strain analysis of structures with rotational degrees of freedom, *Comput. Methods Appl. Mech. Engrg.* 14 (1978) 401–451.
- [10] J. Argyris, An excursion into large rotations, *Comput. Methods Appl. Mech. Engrg.* 32 (1982) 85–155.
- [11] K.J. Bathe, S. Bolourchi, Large displacement analysis of three-dimensional beam structures, *Internat. J. Numer. Methods Engrg.* 14 (1979) 961–986.
- [12] T. Belytschko, L.W. Glaum, Applications of higher order corotational stretch theories to nonlinear finite element analysis, *Comput. Struct.* 10 (1979) 175–182.
- [13] A. Cardona, M. Geradin, A beam finite element non-linear theory with finite rotations, *Internat. J. Numer. Methods Engrg.* 26 (1988) 2403–2438.
- [14] E.N. Dvorkin, E. Onate, J. Oliver, On a non-linear formulation for curved Timoshenko beam elements considering large displacement/rotation increments, *Internat. J. Numer. Methods Engrg.* 26 (1988) 1597–1613.
- [15] M.A. Crisfield, A consistent co-rotational formulation for non-linear, three-dimensional, beam-elements, *Comput. Methods Appl. Mech. Engrg.* 81 (1990) 131–150.
- [16] A. Ibrahimbegović, On the choice of finite rotation parameters, *Comput. Methods Appl. Mech. Engrg.* 149 (1997) 49–71.
- [17] F. Gruttmann, W. Wagner, Finite element analysis of Saint–Venant torsion problem with exact integration of the elasto-plastic constitutive equations, *Comput. Methods Appl. Mech. Engrg.* 190 (2001) 3831–3848.
- [18] A. Dutta, D.W. White, Large displacement formulation of a three-dimensional beam element with cross-sectional warping, *Comput. Struct.* 45 (1992) 9–24.
- [19] J.C. Simo, L. Vu-Quoc, A geometrically-exact rod model incorporating shear and torsion-warping deformation, *Int. J. Solids Struct.* 27 (1991) 371–393.
- [20] Y.L. Pi, N.S. Trahair, Inelastic torsion of steel I-beams, *J. Struct. Eng. (ASCE)* 121 (4) (1995) 609–620.
- [21] E. Zupan, M. Saje, D. Zupan, The quaternion-based three-dimensional beam theory, *Comput. Methods Appl. Mech. Engrg.* 198 (2009) 3944–3956.
- [22] Y.L. Pi, M.A. Bradford, B. Uy, A spatially curved-beam element with warping and Wagner effects, *Internat. J. Numer. Methods Engrg.* 63 (2005) 1342–1369.
- [23] J. Wackerfuß, F. Gruttmann, A mixed hybrid finite beam element with an interface to arbitrary three-dimensional material models, *Comput. Methods Appl. Mech. Engrg.* 198 (2009) 2053–2066.
- [24] F. Mohri, N. Dami, M.P. Ferry, Large torsion finite element model for thin-walled beams, *Comput. Struct.* 86 (2008) 671–683.
- [25] E.J. Sapountzakis, J.A. Dourakopoulos, Lateral buckling analysis of beams of arbitrary cross section by BEM, *Comput. Mech.* 45 (2009) 11–21.
- [26] C. Basaglia, D. Camotim, N. Silvestre, Post-buckling analysis of thin-walled steel frames using generalized beam theory (GBT), *Thin-Wall Struct.* 62 (2013) 229–242.
- [27] J. Frischkorn, S. Reese, A solid-beam finite element and non-linear constitutive modelling, *Comput. Methods Appl. Mech. Engrg.* 265 (2013) 195–212.
- [28] C. Basaglia, D. Camotim, N. Silvestre, Torsion warping transmission at thin-walled frame joints: kinematics, modelling and structural response, *J. Constr. Steel Res.* 63 (2007) 709–717.
- [29] J. Wackerfuß, F. Gruttmann, A nonlinear Hu–Washizu variational formulation and related finite-element implementation for spatial beams with arbitrary moderate thick cross-sections, *Comput. Methods Appl. Mech. Engrg.* 200 (2011) 1671–1690.
- [30] P.S. Lee, G. McClure, A general three-dimensional *L*-section beam finite element for elastoplastic large deformation analysis, *Comput. Struct.* 84 (2006) 215–229.
- [31] P.S. Lee, H.C. Noh, Inelastic buckling behavior of steel members under reversed cyclic loading, *Eng. Struct.* 32 (2010) 2579–2595.
- [32] Z.X. Li, A co-rotational formulation for 3D beam element using vectorial rotational variables, *Comput. Mech.* 39 (2007) 309–322.
- [33] M. Schulz, F.C. Filippou, Non-linear spatial Timoshenko beam element with curvature interpolation, *Internat. J. Numer. Methods Engrg.* 50 (2001) 761–785.
- [34] M. Živković, M. Kojić, R. Slavković, N. Grujović, A general beam finite element with deformable cross-section, *Comput. Methods Appl. Mech. Engrg.* 190 (2001) 2651–2680.
- [35] K. Yoon, Y.G. Lee, P.S. Lee, A continuum mechanics based beam finite element with warping displacements and its modeling capabilities, *Struct. Eng. Mech.* 43 (2012) 411–437.
- [36] K. Yoon, P.S. Lee, Modeling the warping displacements for discontinuously varying arbitrary cross-section beams, *Comput. Struct.* 131 (2014) 56–69.
- [37] M.A. Crisfield, G. Jelenić, Objectivity of strain measures in the geometrically exact three-dimensional beam theory and its finite-element implementation, *Proc. R. Soc.* 455 (1999) 1125–1147.
- [38] A. Cardona, M. Geradin, A beam finite element non-linear theory with finite rotation, *Internat. J. Numer. Methods Engrg.* 26 (1988) 2403–2438.
- [39] A. Ibrahimbegović, F. Frey, I. Kozar, Computational aspects of vector-like parametrization of three-dimensional finite rotations, *Internat. J. Numer. Methods Engrg.* 38 (1995) 65–3673.
- [40] Ritto-Corrêa, D. Camotim, On the differentiation of the Rodrigues formula and its significance for the vector-like parameterization of Reissner–Simo beam theory, *Internat. J. Numer. Methods Engrg.* 55 (2002) 1005–1032.
- [41] P.S. Lee, H.C. Noh, C.K. Choi, Geometry dependent MITC method for a 2-node iso-beam element, *Struct. Eng. Mech.* 29 (2008) 203–221.
- [42] K.J. Bathe, P.S. Lee, J.F. Hiller, Towards improving the MITC9 shell element, *Comput. Struct.* 81 (2003) 477–489.

- [43] P.S. Lee, K.J. Bathe, Development of MITC isotropic triangular shell finite elements, *Comput. Struct.* 82 (2004) 945–962.
- [44] Y.G. Lee, K. Yoon, P.S. Lee, Improving the MITC3 shell finite element by using the Hellinger–Reissner principle, *Comput. Struct.* 110–111 (2012) 93–106.
- [45] H.M. Jeon, P.S. Lee, K.J. Bathe, The MITC3 shell finite element enriched by interpolation covers, *Comput. Struct.* 134 (2014) 128–142.
- [46] E.A.S. Neto, D. Perić, D.R.J. Owen, *Computational Method for Plasticity: Theory and Applications*, Wiley & Sons, 2008.
- [47] ADINA R&D, *ADINA theory and modeling guide*, Watertown, MA: ADINA R&D, 2013.
- [48] ANSYS Inc., *Theory reference-Large deformation analysis*, ANSYS user's manual, 2012.
- [49] J.C. Simo, L. Vu-Quoc, A three-dimensional finite strain rod model. Part II: computational aspects, *Comput. Methods Appl. Mech. Engrg.* 58 (1986) 79–116.
- [50] G. Jelenić, M.A. Crisfield, Geometrically exact 3D beam theory: implementation of a strain invariant finite element for statics and dynamics, *Comput. Methods Appl. Mech. Engrg.* 171 (1999) 141–171.
- [51] J.M. Andeson, N.S. Trahair, Stability of monosymmetric beams and cantilevers, *J. Struct. Div. (ASCE)* 98 (1972) 2647–2662.
- [52] J.M. Battini, *Co-rotational Beam Elements in Instability Problems*, Technical Report, Royal Institute of Technology, Stockholm, 2002.